Article

Cell Host & Microbe

Coronavirus protein interaction mapping in bat and human cells reveals network rewiring governing immune evasion and zoonotic potential

Graphical abstract

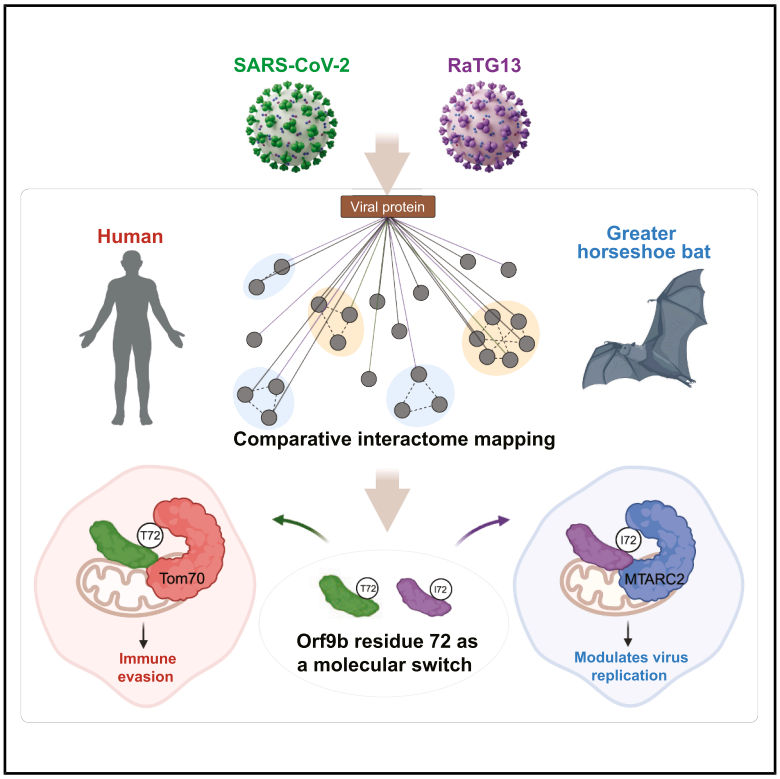

Authors

Jyoti Batra, Magdalena Rutkowska, Yuan Zhou, ..., Lisa Miorin, Adolfo García-Sastre, Nevan J. Krogan

Correspondence

lisa.miorin@mssm.edu (L.M.), adolfo.garcia-sastre@mssm.edu (A.G.-S.), nevan.krogan@ucsf.edu (N.J.K.)

In brief

Batra et al. generate comparative coronavirus-host interaction maps in human and bat cells, identifying conserved and species-specific networks. They show that a single amino acid change in a viral accessory protein can rewire host interactions, uncovering a mechanism that potentially contributes to host adaptation and cross-species transmission.

Highlights

- Human-bat interactomes reveal conserved and host-specific sarbecovirus PPIs
- A single N mutation enables SARS-CoV-2 replication in greater horseshoe bat cells
- Orf9b residue 72 acts as a molecular switch for host targeting across species
- Minimal viral sequence variation reshapes host adaptation and species barriers

Batra et al., 2026, Cell Host & Microbe *34*, 1–18
June 10, 2026
https://doi.org/10.1016/j.chom.2026.04.015

CellPress

Please cite this article in press as: Batra et al., Coronavirus protein interaction mapping in bat and human cells reveals network rewiring governing immune evasion and zoonotic potential, Cell Host & Microbe (2026), https://doi.org/10.1016/j.chom.2026.04.015

Cell Host & Microbe

CellPress
OPEN ACCESS

Article

Coronavirus protein interaction mapping in bat and human cells reveals network rewiring governing immune evasion and zoonotic potential

Jyoti Batra,[1,2,3,4,31] Magdalena Rutkowska,[5,6,31] Yuan Zhou,[1,2,3,4] Chengjin Ye,[7] Rithika Adavikolanu,[1,2,3,4] Janet M. Young,[8] Durga Anand,[1,2,3,4] Sooraj Verma,[1,2,3,4] Haripriya Parthasarathy,[1,2,3,4] Martin Gordon,[1,2,3,4] Shivali Malpotra,[1,2,3,4] Anastasija Cupic,[5,6] Thomas Kehrer,[5] Melanie Dos Santos,[9] Ronald Benjamin,[1,2,3,4] Jack M. Moen,[1,2,3,4] Declan M. Winters,[10,11] Vincent Caval,[12] Ajda Rojc,[1,2,3,4] Ignacio Mena,[5,13,14] Sadaf Aslam,[5] Carles Martinez-Romero,[5,13,15] Isabela Conde Viñas,[5,13] Zain Khalil,[16] Keith Farrugia,[16] Fernando Villalón-Letelier,[5] Atoshi Banerjee,[1,2,3,4] Dafna Tussia-Cohen,[17] Amy Diallo,[2,3] Sourobh Maji,[2,3] Monita Muralidharan,[1,2,3,4] Helene Foussard,[1,2,3,4] Irene P. Chen,[1,3,18] Rotem Fuchs,[17] C.J. San Felipe,[2,3] Lorena Zuliani-Alvarez,[1,2,3,4] Promisree Choudhury,[1,2,3,4] Kirsten Obernier,[1,2,3,4] Ségolène Gracias,[12]

(Author list continued on next page)

[1]J. David Gladstone Institutes, San Francisco, CA 94158, USA
[2]Quantitative Biosciences Institute (QBI), University of California, San Francisco, San Francisco, CA 94158, USA
[3]QBI Coronavirus Research Group (QCRG), University of California, San Francisco, San Francisco, CA 94158, USA
[4]Department of Bioengineering and Therapeutic Sciences, University of California, San Francisco, San Francisco, CA 94158, USA
[5]Department of Microbiology, Icahn School of Medicine at Mount Sinai, New York, NY 10029, USA
[6]Graduate School of Biomedical Sciences, Icahn School of Medicine at Mount Sinai, New York, NY 10029, USA
[7]Texas Biomedical Research Institute, San Antonio, TX 78227, USA
[8]Division of Basic Sciences, Fred Hutchinson Cancer Center, Seattle, WA 98109, USA
[9]Interactomics, RNA and Immunity Laboratory, Institut Pasteur, Université Paris Cité, Paris 75015, France
[10]Department of Microbiology, Immunology, and Molecular Genetics (MIMG), University of California, Los Angeles, Los Angeles, CA 90024, USA
[11]Institute for Quantitative and Computational Biosciences (QCBio), University of California, Los Angeles, Los Angeles, CA 90024, USA
[12]Institut Pasteur, Université Paris Cité, CNRS UMR 3569, Virus sensing and signaling Unit, Paris 75015, France
[13]Global Health Emerging Pathogens Institute, Icahn School of Medicine at Mount Sinai, New York, NY 10029, USA
[14]The Scripps Research Institute, Immunology and Microbiology Department, La Jolla, CA 92037, USA

(Affiliations continued on next page)

SUMMARY

Coronaviruses, including severe acute respiratory syndrome coronavirus 2 (SARS-CoV-2), can cause severe disease in humans, whereas reservoir hosts such as horseshoe bats remain asymptomatic. To investigate how host-specific protein-protein interactions (PPIs) influence infection, we generated comparative PPI maps for SARS-CoV-2 and its bat progenitor RaTG13, using affinity purification mass spectrometry (AP-MS) in human and greater horseshoe bat cells. We identify both conserved and virus- and host-specific interactions that regulate infection dynamics. Notably, SARS-CoV-2 requires a nonsynonymous mutation in the nucleocapsid to replicate in bat cells expressing human ACE2 and TMPRSS2. Strikingly, a single amino acid difference in Orf9b between viruses acts as a molecular switch that reprograms mitochondrial targeting: in human cells, enhanced translocase of outer mitochondrial membrane 70 (Tom70) binding promotes immune evasion, whereas in bat cells, strengthened interaction with the bat-enriched restriction factor mitochondrial amidoxime reducing component 2 (MTARC2) limits infection. These findings establish a general principle by which minimal sequence variation can reshape virus-host interactions and contribute to immune antagonism, host adaptation, and species barriers.

INTRODUCTION

Severe acute respiratory syndrome coronavirus 2 (SARS-CoV-2) is the causative agent of the COVID-19 pandemic, which resulted in over 770 million cases and 7 million deaths globally (source: WHO[1]). SARS-related coronaviruses (SARSr-CoVs) have been identified in horseshoe bats[2] and pangolins,[3] although the definitive reservoir of SARS-CoV-2 remains uncertain. Horseshoe bats are considered major natural hosts of SARSr-CoVs, including SARS-CoV, which caused the 2003 outbreak,[4] likely due to unique antiviral defense and inflammatory mechanisms. Horseshoe bats are distributed across Asia, Southern Europe, and North Africa

CellPress
OPEN ACCESS

Cell Host & Microbe
Article

Rahul K. Suryawanshi,[1,19] Boris Bonaventure,[5] Carlos Ibáñez,[20] Jeffrey R. Johnson,[5,13] Javier Juste,[20,21] Lars Pache,[22] Robert M. Stroud,[2,3] Kliment A. Verba,[2,3] James S. Fraser,[2,3] Harm van Bakel,[5,16,23,24] Taha Y. Taha,[1,4] Melanie Ott,[1,2,3,18,25] Tzachi Hagai,[17] Nolwenn Jouvenet,[12] Caroline Demeret,[9] Benjamin J. Polacco,[1,2,3,4] Danielle L. Swaney,[1,2,3,4] Ignacia Echeverria,[2,3,4] Mehdi Bouhaddou,[10,11] Manon Eckhardt,[1,2,3,4] Harmit S. Malik,[8,26] Luis Martinez-Sobrido,[7] Lisa Miorin,[5,13,*] Adolfo García-Sastre,[5,13,27,28,29,30,*] and Nevan J. Krogan[1,2,3,4,32,*]

[15]Memorial Sloan Kettering Cancer Center, New York, NY 10065, USA
[16]Department of Genetics and Genomic Sciences, Icahn School of Medicine at Mount Sinai, New York, NY 10029, USA
[17]Shmunis School of Biomedicine and Cancer Research, George S Wise Faculty of Life Sciences, Tel Aviv University, Tel Aviv 6997801, Israel
[18]Department of Medicine, University of California, San Francisco, San Francisco, CA 94158, USA
[19]Laboratory of Neurological Infections and Immunity, Division of Intramural Research, National Institute of Allergy and Infectious Diseases, Rocky Mountain Laboratories, Hamilton, MT 59840, USA
[20]Estación Biológica de Doñana (CSIC), Avda. Américo Vespucio 26, 41092 Seville, Spain
[21]CIBER Epidemiology and Public Health, CIBERESP, 28029 Madrid, Spain
[22]NCI Designated Cancer Center, Sanford Burnham Prebys Medical Discovery Institute, La Jolla, CA 92037, USA
[23]Icahn Genomics Institute, Icahn School of Medicine at Mount Sinai, New York, NY 10029, USA
[24]Department of Artificial Intelligence and Human Health, Icahn School of Medicine at Mount Sinai, New York, NY 10029, USA
[25]Biohub, San Francisco, CA 94158, USA
[26]Howard Hughes Medical Institute, Fred Hutchinson Cancer Center, Seattle, WA 98109, USA
[27]Department of Medicine, Division of Infectious Diseases, Icahn School of Medicine at Mount Sinai, New York, NY 10029, USA
[28]The Tisch Cancer Institute, Icahn School of Medicine at Mount Sinai, New York, NY 10029, USA
[29]The Icahn Genomics Institute, Icahn School of Medicine at Mount Sinai, New York, NY 10029, USA
[30]Department of Pathology, Molecular and Cell-Based Medicine, Icahn School of Medicine at Mount Sinai, New York, NY 10029, USA
[31]These authors contributed equally
[32]Lead contact
*Correspondence: lisa.miorin@mssm.edu (L.M.), adolfo.garcia-sastre@mssm.edu (A.G.-S.), nevan.krogan@ucsf.edu (N.J.K.)
https://doi.org/10.1016/j.chom.2026.04.015

but are absent in the Americas. The two SARSr-CoVs RaTG13 and BANAL-52, identified in intermediate horseshoe bat (*R. affinis*)[5] and Malayan horseshoe bat (*R. malayanus*),[2] respectively, are among the closest relatives of SARS-CoV-2, sharing 96.2% and 96.8% genome-wide identity, respectively. BANAL-52 shows a higher similarity in the spike receptor-binding domain (RBD), correlating with stronger human angiotensin converting enzyme 2 (hACE2) binding and enhanced virus entry into human cells compared with that of RaTG13.[2] Despite the high prevalence of SARSr-CoVs in bats, the molecular determinants of cross-species transmission and mechanisms underlying asymptomatic infection remain poorly understood. Therefore, studying host-virus interactions in bat reservoirs is critical to understanding coronavirus biology and spillover. However, few bat cell lines support productive SARS-CoV-2 infection,[6–9] posing a significant barrier to studying the mechanisms that facilitate SARS-CoV-2 spillover events. Here, we report the establishment of a lung fibroblast cell line from greater horseshoe bats (*R. ferrumequinum*), which we call RFe. To investigate how host interactions impact viral infection, we engineered RFe cells to express hACE2 and human transmembrane serine protease 2 (hTMPRSS2) (referred to as RFe-AT) and selected a SARS-CoV-2 variant capable of efficient replication in bat cells. This process identified a single-nucleocapsid mutation (N_P80T) that is sufficient for productive replication in RFe-AT cells. Our bat infection model provides a platform to study coronavirus-host co-evolution and bat-specific antiviral responses.

Since successful viral replication depends on protein-protein interactions (PPIs) between viral and host proteins, we reasoned that comparative interactome analyses in bat and human cells could reveal host-specific factors governing viral replication and immune evasion. Indeed, previous SARS-CoV-2-human PPI studies have provided key mechanistic insights into host responses to infection.[10–12] Thus, identifying conserved and divergent interactions across species could uncover pathways critical for viral infection, adaptation, and zoonotic transmission. Using affinity purification mass spectrometry (AP-MS), we mapped protein interactions of RaTG13 and SARS-CoV-2 viral proteins in RFe and human HEK293T cells, identifying conserved and species-specific host interactions. Our previous findings showed that SARS-CoV-2 Orf9b, an accessory protein translated from an alternative open reading frame (ORF) within N gene, is implicated in innate immune evasion by targeting Tom70 (translocase of outer mitochondrial membrane 70). In contrast, RaTG13 Orf9b exhibited a reduced interaction with Tom70, resulting in diminished suppression of innate immune response. We generated a recombinant SARS-CoV-2 carrying a mutation in Orf9b that disrupts Tom70 binding. This mutant virus was attenuated in both bat and human cells, leading to a heightened immune response. Conversely, RaTG13 Orf9b preferentially binds to another mitochondrial protein MTARC2 (mitochondrial amidoxime reducing component 2), specifically in bat cells. We showed that MTARC2 is a bat-specific restriction factor that suppresses SARS-CoV-2 replication. Therefore, our findings reveal distinct mechanisms of immune modulation and viral persistence between human and bat hosts. Additionally, we identified several unique interactions in bat cells that suggest other distinct mechanisms underlying immune modulation and viral persistence. Overall, our findings advance the understanding of how SARS-CoV-2 and related viruses adapt to distinct hosts and evade immunity, informing strategies to combat these pathogens.

RESULTS

Comparative interactome profiling of SARS-CoV-2 and RaTG13 in bat and human cells reveals conserved and virus-specific interactions

Bats serve as natural reservoir hosts for a wide range of emerging viruses, including SARSr-CoVs, yet the molecular

Please cite this article in press as: Batra et al., Coronavirus protein interaction mapping in bat and human cells reveals network rewiring governing immune evasion and zoonotic potential, Cell Host & Microbe (2026), https://doi.org/10.1016/j.chom.2026.04.015

CellPress
OPEN ACCESS

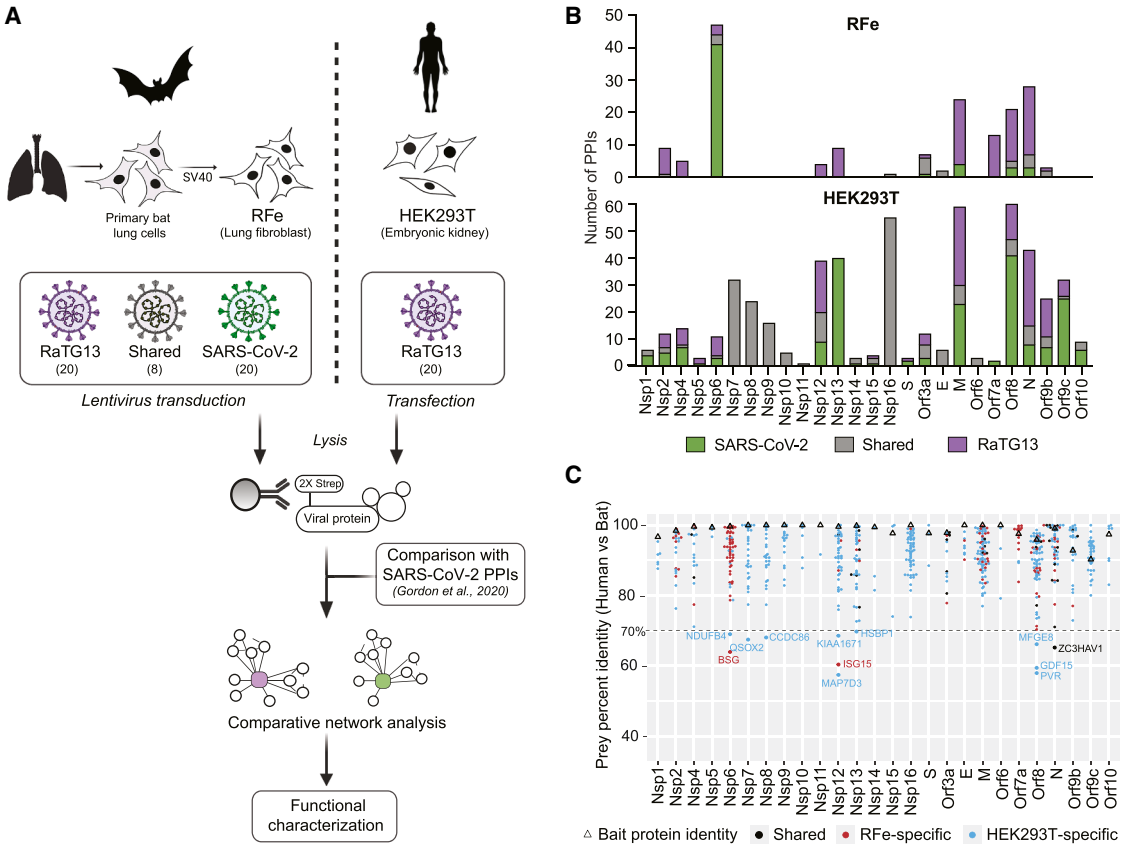

Figure 1. An affinity purification mass spectrometry (AP-MS) approach for comparative network analysis of SARSr-CoVs

(A) Schematic overview of the affinity purification coupled to AP-MS workflow for mapping protein-protein interactions (PPIs) of SARS-CoV-2 and RaTG13 in human (HEK293T) and bat (RFe) cells.

(B) Bar plot showing the number of high-confidence PPIs identified for each viral protein of SARS-CoV-2 and RaTG13 in RFe (top) and HEK293T (bottom) cells. Interactions are color-coded as SARS-CoV-2-specific (green), RaTG13-specific (purple), or shared (gray).

(C) Dot plot showing the percent sequence identity between human (HEK293T) and bat (RFe) orthologs for all PPIs, grouped by viral bait. Each dot represents a prey identified with either RaTG13 or SARS-CoV-2 viral baits.

mechanisms that govern coronavirus replication and host restriction in bat cells remain poorly defined. To investigate these mechanisms, we sought to develop an *in vitro* model to study host-virus interactions and characterize cellular response to SARS-CoV-2 infection in a bat-host context. To date, most SARSr-CoVs have been identified in horseshoe bats. Therefore, we focused on developing a SARS-CoV-2 infection model using cell lines derived from the lung tissue of a greater horseshoe bat captured in southern Spain in 2020. Primary fibroblasts were established from adult male bat lung tissue, following enzymatic and mechanical dissociation, and cultured to allow outgrowth. The cells were then expanded and immortalized with SV40 large T antigen. These immortalized bat lung fibroblast cells are referred to as RFe cells throughout this study. To confirm species origin, we compared cytochrome b and c gene sequences from RNA sequencing (RNA-seq) with published NCBI Reference Sequences,[13] confirming >99.5% identity (Table S1). By abundance proteomics, we identified common lung fibroblast markers, including S100 calcium-binding protein A4 (S100A4), vimentin (VIM), and collagen proteins, which were prominently detected in both bat and human lung fibroblast cells (RFe and MRC5 cells, respectively) compared with the human embryonic kidney cell line (HEK293T), as expected (Figure S1A). Additionally, similar to MRC5 cells, immortalized RFe cells displayed typical fibroblast morphology, including large, spindle-shaped cells with oval nuclei (Figure S1B).

Leveraging these cell lines and extending our previous work on SARS-CoV-2 interactome in HEK293T cells,[12] we systematically mapped host factors interacting with individual proteins from SARS-CoV-2 and RaTG13 in both RFe (bat) and HEK293T (human) cells. SARS-CoV-2 and RaTG13 share high sequence similarity, with 8 viral proteins (Nsp7-11, Nsp16, E and Orf6) being 100% identical at the amino acid level (Figure S2A). For interactome mapping, we codon-optimized each viral gene and cloned them into mammalian expression vectors, pLVX-EF1a and pLVX-TetOne, with a 2x-Strep tag. The pLVX-EF1a viral constructs were expressed in HEK293T cells by transient transfection. Due to low transfection efficiency in bat cells, we generated stable cells for each protein using the doxycycline-inducible pLVX-TetOne system. Each viral protein was affinity-purified, and interacting host factors were identified using MS. High-confidence interactions were determined using SAINTexpress

Please cite this article in press as: Batra et al., Coronavirus protein interaction mapping in bat and human cells reveals network rewiring governing immune evasion and zoonotic potential, Cell Host & Microbe (2026), https://doi.org/10.1016/j.chom.2026.04.015

(significance analysis of interactome)[14] and MiST (mass spectrometry interaction statistics)[15] scoring algorithms (Figure 1A).

Using this approach, we identified 72 high-confidence PPIs of SARS-CoV-2 in RFe cells, as well as 118 and 189 interactors of RaTG13 in RFe and HEK293T cells, respectively (Figure 1B; Table S2). Previously, we described 332 high-confidence PPIs of SARS-CoV-2 in HEK293T cells.[12] Orf3b and Orf7b were excluded from analysis due to the unusually high number of background PPIs. Notably, Nsp6 and Orf7a showed higher numbers of PPIs in RFe compared with HEK293T cells. We observed fewer SARS-CoV-2 PPIs than RaTG13 in bat cells, likely due to lower expression of SARS-CoV-2 baits, as indicated by $\log_2$ intensity values and western blot (Figures S2B–S2E), resulting in reduced host protein enrichment and fewer detectable interactions.

Despite their high similarity, we identified distinct interactomes for SARS-CoV-2 and RaTG13, with only 14% and 10% shared interactions in HEK293T and RFe cells, respectively (Figure S2F). For RaTG13, ~9% of interactions were conserved across bat and human cells. To further investigate species-specific differences, we analyzed the sequence identity of host proteins interacting with SARS-CoV-2 and/or RaTG13 between bat and human orthologs. While most interactors were highly conserved, a subset of species-specific interactions involved prey proteins with lower sequence identity, including interactors of Orf8 and Nsp12 (Figure 1C; Table S3). These divergent orthologs may underlie functional differences in how viral proteins engage host pathways in bats versus humans, potentially shaping species-specific outcomes of infection and immune modulation. Notably, Zinc-finger antiviral protein ZC3HAV1 (zinc finger CCCH-type containing, antiviral 1 protein, referred to below as ZAP) stood out as a shared interactor with RaTG13 N in both species. ZAP is an antiviral effector that promotes viral RNA degradation.[16] Its rapid evolution in primates[17] and low sequence identity between human and bat orthologs suggest that despite conserved binding, sequence divergence may underlie species-specific differences in antiviral activity.

To quantitatively compare SARS-CoV-2 and RaTG13 PPIs, we applied our previously developed differential interaction scoring (DIS) method[18] to identify conserved and virus-specific interactions across HEK293T and RFe cells (Figures 2 and S3). Comparative interactome mapping identified conserved host interactions, along with virus- and host-specific differences indicative of evolutionary adaptation and differential targeting of host pathways. In both host systems, viral proteins targeted key cellular pathways, including RNA processing (Nop56p-associated pre-rRNA complex), translation (regulation of gene expression), trafficking (nuclear/mitochondrial transport), and innate immune regulation (Tom70, stress granule regulation). For example, N proteins of both viruses interact with the Nop56p-associated pre-rRNA complex (Figure S3), suggesting a conserved role in modulating host gene expression in both cell types. Similarly, Orf8 of both viruses interacted with factors involved in ER organization and protein quality control in both species, consistent with prior reports showing Orf8 accumulation in the ER and its role in ER remodeling.[19] We also noticed several virus-specific interactions, including SARS-CoV-2 Nsp4 binding to the Translocase of the Inner Membrane (TIM) (translocase of the inner membrane) complex in human cells, whereas RaTG13 Nsp12 binds to components of the microtubule-organizing center (MTOC) (Figure 2B). We also observed a bat-specific interaction between RaTG13 Nsp2 and flotillin proteins (FLOT1/2), indicating potential divergence in targeting of membrane-associated trafficking pathways across species (Figure S3A).

RaTG13 was detected in intermediate horseshoe bats, but due to unavailability of corresponding bat cell models, we performed our studies in greater horseshoe cells, which diverged ~16–17 million years ago. To assess cross-species compatibility, we performed a genome-wide orthology analysis between greater and intermediate bats and identified likely one-to-one orthologs for 18,601 of 19,533 genes (95.2%), including all 171 AP-MS host factors (Figure S4A). These orthologs showed high conservation, with a median protein identity of 98.1% (99.0% for AP-MS preys) (Figures S4B and S4C), supporting the use of greater horseshoe bat cells as a suitable surrogate for studying interactions relevant to the intermediate horseshoe host background of RaTG13.

Some of the host- or virus-specific interactions might result from increased sensitivity of immunoprecipitations due to differences in viral and host protein expression, or to peculiarities of the used cell lines. Although the lack of a matched human respiratory epithelial model limits direct dissection of species- versus cell-type-specific effects, most interactors were expressed at comparable levels in HEK293T and MRC5 cells (Figure S4D), suggesting that observed interaction differences are unlikely to be driven by differences in cell-line-specific expression. Nevertheless, these comparative interactome maps across bat and human cells delineate conserved and host-specific interactions exploited by sarbecoviruses. This dataset is likely to include virus-specific interactions that influence host tropism, immune evasion, and cross-species transmission. Thus, our data provide valuable information to further validate the identified host and viral factors involved in sarbecovirus spillovers from bats to humans.

Differential interaction of Orf9b from SARS-CoV-2 and RaTG13 with mitochondrial proteins Tom70 and MTARC2

To further investigate virus- and host-specific differences, we examined the distribution of global DIS scores (Figures 3A and 3B). In agreement with our earlier findings (Figure S2F), DIS values for cross-host species comparisons were enriched near ±1, indicating a higher divergence (Figure 3A, light and dark blue), whereas SARS-CoV-2 versus RaTG13 comparisons within the same hosts were closer to zero, indicating more shared interactions (Figure 3A, red and orange). This analysis revealed virus-specific and/or host-specific enrichment, including a RaTG13-specific interaction of Orf7a with nuclear transport factors (i.e., CSE1L, NUP205, NUP93, TNPO1, and XPO1) in both cells (Figure 3B). Several bat-specific interactions were identified, such as interferon-stimulated gene (ISG)15, SCARB1, and PRDX3, which suggest distinct immune modulation strategies[23–26] or mechanisms of viral persistence in bat hosts (Figures 3B and S5A). To investigate whether the absence of these interactions in HEK293T cells is due to differential protein abundance, we performed deep proteome profiling. Interestingly, many bat-specific proteins (e.g., NIFK, PRDX3, SCARB1, BSG, and MTARC2) were expressed at comparable

Please cite this article in press as: Batra et al., Coronavirus protein interaction mapping in bat and human cells reveals network rewiring governing immune evasion and zoonotic potential, Cell Host & Microbe (2026), https://doi.org/10.1016/j.chom.2026.04.015

CellPress
OPEN ACCESS

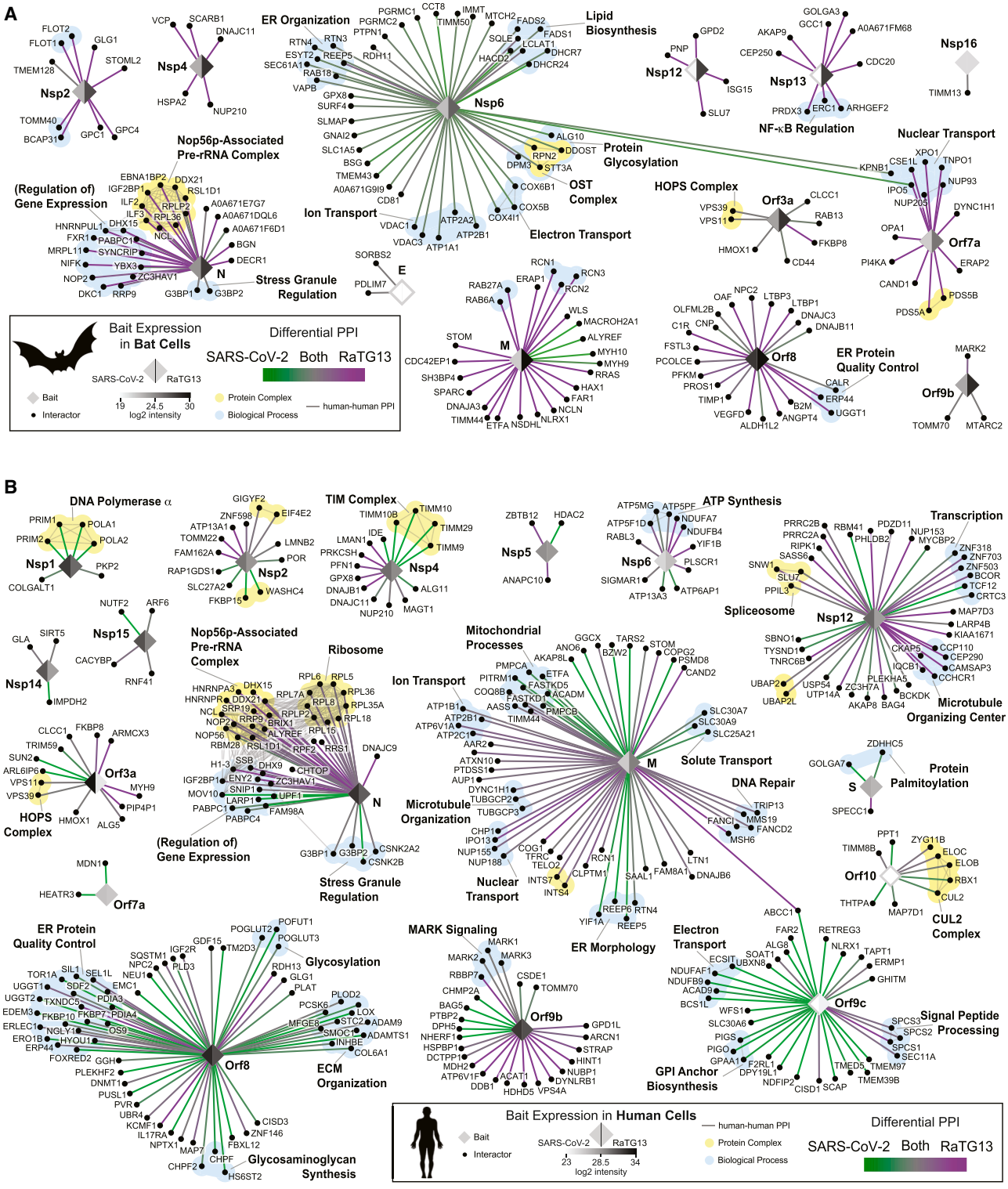

Figure 2. Conserved and distinct host-virus interaction landscapes of SARS-CoV-2 and RaTG13

(A) Comparative differential interaction map depicting SARS-CoV-2-RaTG13 comparison of bat-virus interactions. Edge color represents the DIS scores: green and purple indicate SARS-CoV-2- and RaTG13-specific interactions, respectively, gray indicates shared interactions. Each bait node is split to show $\log_2$ expression levels for SARS-CoV-2 (left) and RaTG13 (right). Thin gray edges indicate known host-host (human-human) interactions. Host proteins within the same complex or biological process are highlighted in yellow and blue, respectively, based on databases (CORUM[20], GO[21,22]), and literature curation.

(B) Comparative differential interaction map depicting virus-host interactions for SARS-CoV-2 and RaTG13 in human cells.

Please cite this article in press as: Batra et al., Coronavirus protein interaction mapping in bat and human cells reveals network rewiring governing immune evasion and zoonotic potential, Cell Host & Microbe (2026), https://doi.org/10.1016/j.chom.2026.04.015

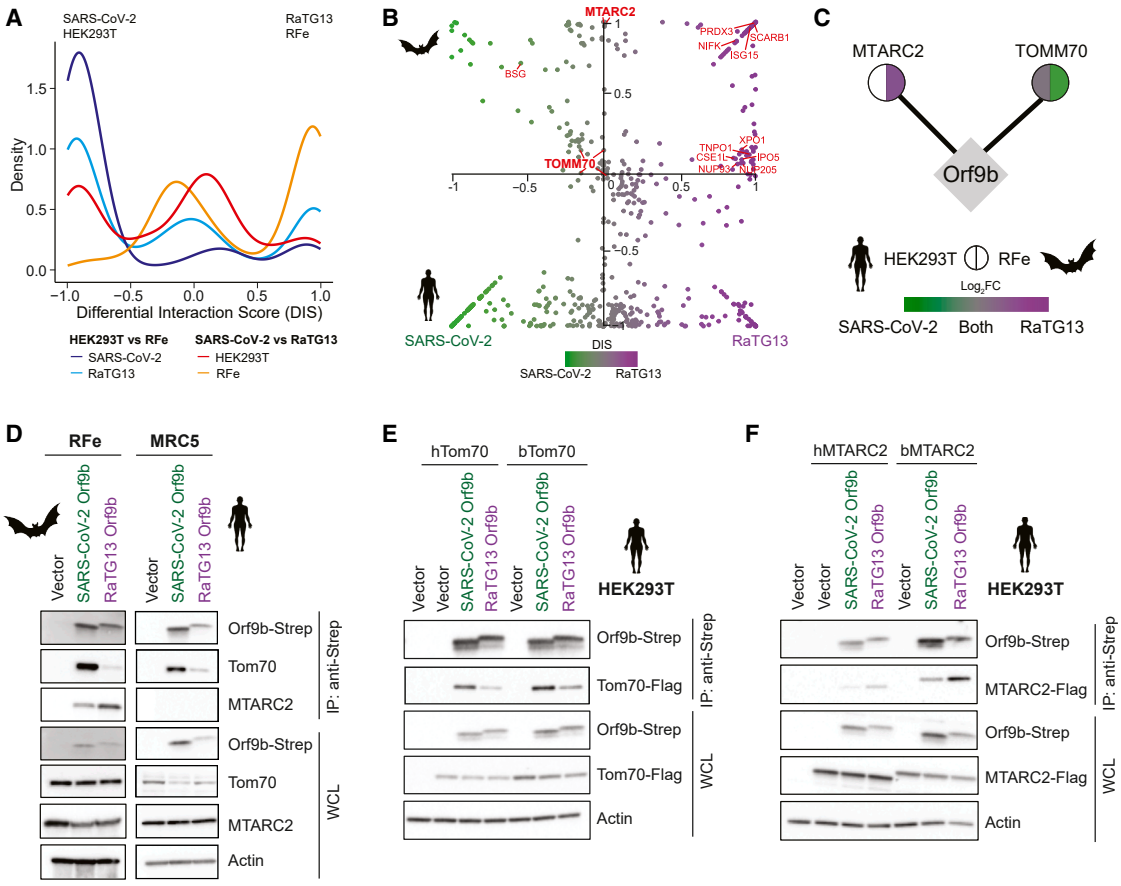

Figure 3. Differential interaction of SARS-CoV-2 and RaTG13 Orf9b with mitochondrial proteins Tom70 and MTARC2 across bats and human

(A) Density histogram representing the distribution of DIS scores comparing SARS-CoV-2 and RaTG13 interactomes within and across HEK293T and RFe cells. PPIs from identical viral baits were excluded from cross-virus comparisons.

(B) Scatterplot of DIS showing virus- and species-specific host protein interactions for SARS-CoV-2 (left) and RaTG13 (right) in bat (top) and human (bottom) cells. Each dot represents a host protein, colored by viral specificity (green for SARS-CoV-2, purple for RaTG13 and gray for shared).

(C) Comparative network of SARS-CoV-2 and RaTG13 Orf9b interactions with Tom70 and MTARC2. Each node represents the host interactor, with split circles indicating enrichment in HEK293T (left) and RFe (right) cells. Node color reflects $\log_2$ fold change ($\log_2$FC) of prey enrichment for RaTG13 versus SARS-CoV-2, based on MSstats analysis: green (SARS-CoV-2-specific), purple (RaTG13-specific), gray (shared), and white (not detected).

(D) Co-immunoprecipitation (coIP) of Strep-tagged Orf9b from SARS-CoV-2 and RaTG13 with endogenous Tom70 or MTARC2 in RFe and MRC5 cells.

(E and F) CoIP of Strep-tagged Orf9b with FLAG-tagged Tom70 (E) or MTARC2 (F) orthologs from human or bat in HEK293T cells.

or higher levels in HEK293T cells (Figure S5A), indicating that factors such as sequence divergence, post-translational modifications, or cell-type-specific complexes likely underlie the interaction differences. When comparing all four datasets, we identified several conserved interactions, underscoring the critical involvement of these shared host proteins and complexes in sarbecovirus infection (Figures 3B and S5B). Notably, the N protein consistently interacted with stress-granule-associated proteins (G3BP1 and G3BP2), a previously characterized interaction known to suppress interferon response.[27] Additionally, we observed a conserved interaction of Orf9b with Tom70 (gene name TOMM70), a mitochondrial import receptor essential for mitochondrial-antiviral protein MAVS (mitochondrial antiviral-signaling protein) signaling, which we previously identified as a direct target of SARS-CoV-2 Orf9b in human cells for suppression of innate immune responses.[18,28]

To uncover functional modules perturbed by each virus, we performed network propagation analysis on PPIs to identify both virus-specific and shared pathway-level signatures. Due to lower bait expression and sparse PPI detection for SARS-CoV-2 in bat cells, we performed this analysis on human datasets, comparing SARS-CoV-2 and RaTG13 PPIs. Using either virus as a seed in the Reactome functional interaction (FI) network, we identified virus-specific and shared proteins, including candidates that were not detected in the PPI dataset (Figure S6A). Notably, SARS-CoV-2 showed strong enrichment for mitochondrial pathways, including oxidative phosphorylation, ATP synthesis, electron transport, and mitochondrial localization (Figure S6B). To pinpoint viral proteins potentially driving the observed mitochondrial pathway associations, we performed network propagation separately for each viral protein and quantified the associations with mitochondrial Gene Ontology (GO) terms. This analysis highlighted SARS-CoV-2 Orf9b and Nsp4 as the top candidates, consistent with previous reports implicating SARS-CoV-2 Orf9b in the modulation of mitochondrial function and antiviral signaling.[28,29] In contrast, RaTG13 Orf9b

Please cite this article in press as: Batra et al., Coronavirus protein interaction mapping in bat and human cells reveals network rewiring governing immune evasion and zoonotic potential, Cell Host & Microbe (2026), https://doi.org/10.1016/j.chom.2026.04.015

CellPress
OPEN ACCESS

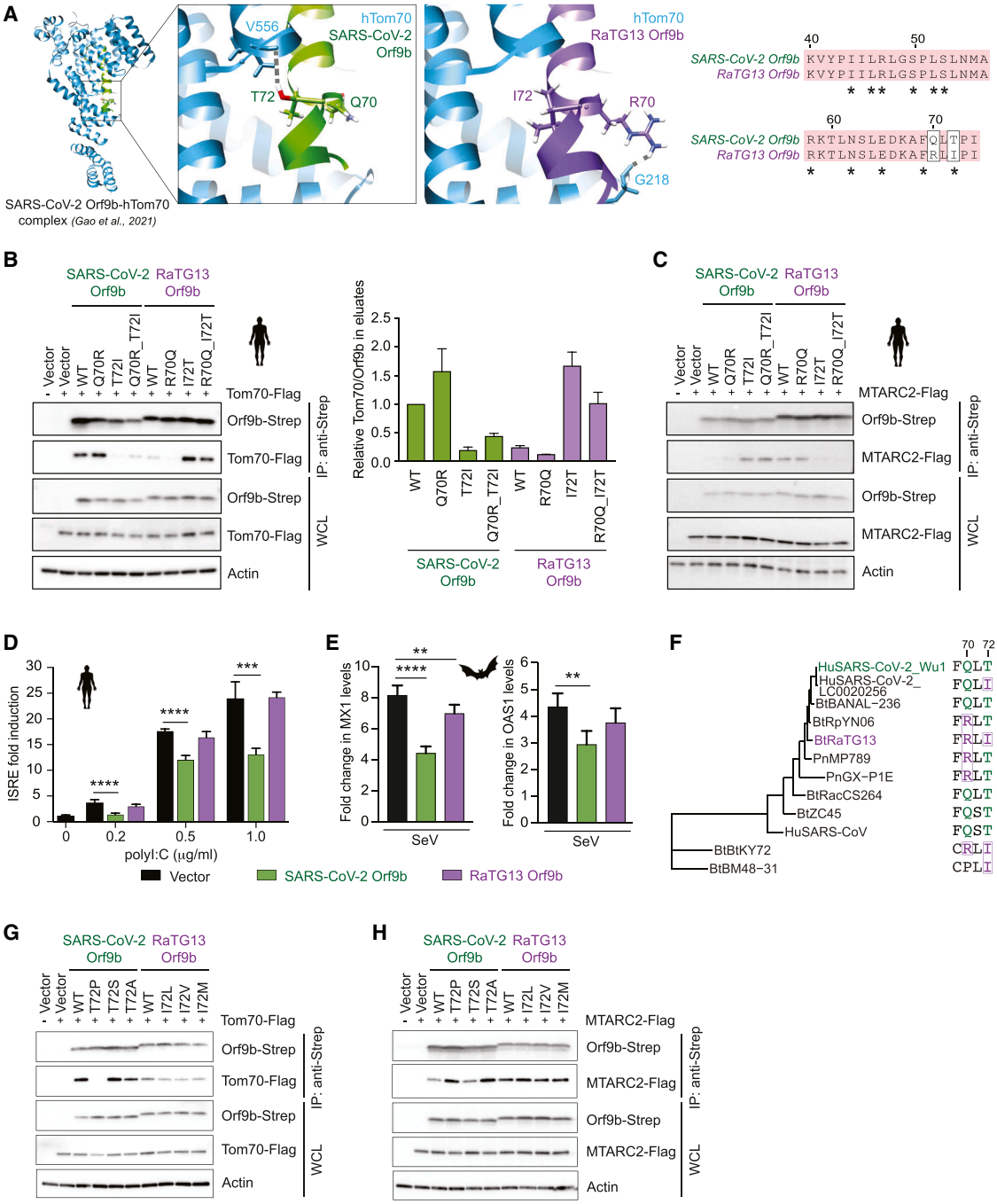

Figure 4. Molecular switch at residue 72 in Orf9b governs interactions with Tom70 and MTARC2 to modulate antiviral response

(A) Comparative structural modeling of RaTG13 Orf9b (purple) bound to hTom70, using the crystal structure of SARS-CoV-2 Orf9b (green) in complex with hTom70 as a template. Hydrogen bonds are shown as gray dashed lines. The right panel shows sequence alignment of SARS-CoV-2 and RaTG13 Orf9b; conserved residues are shaded in red; asterisks indicate Tom70-interacting residues in SARS-CoV-2 Orf9b. Residues at positions 70 and 72 (boxed) were selected for mutational analysis.

(B) CoIP of Strep-tagged Orf9b mutants with FLAG-tagged Tom70 in HEK293T cells (left). Bar graph (right) shows densitometric quantification of Tom70 co-precipitation normalized to Orf9b levels, averaged from biological replicates (mean ± SD).

(C) CoIP of FLAG-tagged MTARC2 with SARS-CoV-2 and RaTG13 Orf9b wild type and mutants in HEK293T cells.

(D) Interferon-stimulated response element (ISRE) reporter activity in HEK293T cells expressing Orf9b at varying poly(I:C) concentrations. Fold activation was calculated relative to unstimulated cells.

(E) Fold change in Sendai virus (SeV)-induced Mx1 and OAS1 expression in bat cells expressing Orf9b or vector control, measured by RT-qPCR relative to uninfected cells. Data are presented as mean ± SD, *n* = 3).

(legend continued on next page)

Please cite this article in press as: Batra et al., Coronavirus protein interaction mapping in bat and human cells reveals network rewiring governing immune evasion and zoonotic potential, Cell Host & Microbe (2026), https://doi.org/10.1016/j.chom.2026.04.015

exhibited fewer mitochondrial associations, suggesting potential functional divergence (Figures S6C–S6E). To further explore the interaction landscape of Orf9b, we conducted a separate quantitative and comparative PPI mapping of SARS-CoV-2 and RaTG13 Orf9b in bat and human cells simultaneously (Table S4; see STAR Methods section "Orf9b PPI and MSstats analysis"). This analysis revealed differential binding to mitochondrial proteins Tom70 and MTARC2, particularly in bat cells (Figure 3C). While Orf9b-Tom70 interaction is conserved across viruses in HEK293T cells, SARS-CoV-2 interacts with Tom70 more strongly than RaTG13 in bat cells. Conversely, MTARC2-Orf9b interaction was detected only in bat cells and was enriched for RaTG13 Orf9b. MTARC2 is a mitochondrial amidoxime-reductase involved in lipid metabolism and redox regulation[30,31] and has not been previously described to play a role in viral pathogenesis.

Next, we validated our proteomics findings using co-immunoprecipitation (coIP) assays and confirmed SARS-CoV-2 Orf9b interaction with endogenous Tom70 in both bat (RFe) and human (MRC5 and HEK293T, respectively) cells, whereas RaTG13 Orf9b showed weaker binding (Figures 3D and S7A). Conversely, RaTG13 Orf9b preferentially interacted with endogenous MTARC2 in bat cells, whereas this interaction was weak or undetectable in human cells (Figures 3D and S7A). Bat and human Tom70 and MTARC2 orthologs share 96.88% and 76.72% sequence identity, respectively, whereas Orf9b is 92.78% identical between SARS-CoV-2 and RaTG13. To compare the binding strength of Orf9b across bat and human orthologs, we performed coIPs in HEK293T cells co-expressing Strep-tagged Orf9b and FLAG-tagged Tom70 or MTARC2 from bats or humans. SARS-CoV-2 Orf9b interacted equally with both human and bat Tom70 orthologs, whereas RaTG13 Orf9b showed weaker binding (Figure 3E). In contrast, MTARC2 co-precipitated more strongly with RaTG13 Orf9b compared with SARS-CoV-2 (Figure 3F), with stronger binding to bMTARC2 compared with hMTARC2, consistent with AP-MS results. We further employed an orthogonal, quantitative cell-based approach, Gaussia princeps complementation (GPCA), to assess relative interaction strengths.[32,33] In this assay, Tom70 or MTARC2 orthologs were fused to Glc1 and Orf9b variants to Glc2. Consistent with our coIP findings, GPCA showed reduced binding of RaTG13 Orf9b to both human and bat Tom70 compared with that of SARS-CoV-2 Orf9b, whereas RaTG13 Orf9b showed stronger interaction with bMTARC2 (Figure S7B). MTARC2 expression levels were very low, and hMTARC2 did not express at adequate levels. In conclusion, we observed that Orf9b has switched its preference in binding to Tom70 (SARS-CoV-2) versus MTARC2 (RaTG13), suggesting functional differences in mitochondrial targeting, immune modulation, and host adaptation between the two viruses.

Next, we performed coIPs using matched viral and host orthologs across greater and intermediate horseshoe bats. In addition to RaTG13 Orf9b, we included Orf9b from Rf4092, a bat coronavirus detected in greater horseshoe bats that shares 72.76% identity with SARS-CoV-2 Orf9b.[34] Tom70 is 99.02% identical between the species, while MTARC2 is 90.9% identical (Figure S4C). Rf4092 Orf9b has conserved Tom70-interacting residues (with the exception of N62D) (Figure S7C) and showed comparable Tom70 interaction with SARS-CoV-2 Orf9b (Figure S7D). Consistent with our previous findings, RaTG13 Orf9b showed weaker binding to Tom70 compared with SARS-CoV-2 Orf9b across both species. For MTARC2, the more divergent Rf4092 Orf9b showed no interactions with MTARC2 from either bat species (Figure S7E). Our data suggest that Orf9b derived from distinct sarbecoviruses exhibits a conserved interaction pattern with Tom70 and MTARC2 across greater and intermediate horseshoe bats, indicating that these host-virus interactions are conserved despite evolutionary divergence. However, comparative analyses of Orf9b from different bat-derived sarbecoviruses revealed species-specific differences in interaction strength depending on the viral origin of Orf9b.

Orf9b residue 72 as a molecular switch governing its interactions with Tom70 and MTARC2

We, and others, previously resolved the structure of SARS-CoV-2 Orf9b in complex with the C-terminal domain of hTom70.[18,35] SARS-CoV-2 Orf9b forms a dimer and consists mainly of β sheets (PDB: 6Z4U).[36] However, SARS-CoV-2 Orf9b adopts an α-helical conformation upon binding to the substrate-binding site of Tom70 in a 1:1 stoichiometry,[35] and this complex is stabilized by hydrogen bonding and hydrophobic interactions. Using these structures as templates, we utilized homology modeling to predict the binding interface between RaTG13 Orf9b and hTom70 and compared the contact residues and binding properties. In SARS-CoV-2 Orf9b, T72 is situated in a hydrophobic pocket of Tom70, engaging in extensive hydrophobic interactions and forming a hydrogen bond with Tom70 V556,[35] whereas the corresponding I72 in RaTG13 Orf9b does not (Figure 4A). Instead, RaTG13 Orf9b R70 forms a hydrogen bond with Tom70 G218. Secondary structure predictions[37] indicate that RaTG13 variant (R70/I72) exhibits an extended α helix compared with SARS-CoV-2 (Q70/T72), suggesting that these substitutions modestly enhance local helical propensity (Figure S8A), which may contribute to their distinct Tom70-binding properties.

To explore these structural differences, we generated Orf9b point mutants and assessed Tom70 binding by coIP. In SARS-CoV-2 Orf9b, Q70R did not change the interaction, whereas T72I markedly reduced Tom70 binding. Conversely, I72T alone or with R70Q in RaTG13 restored Tom70 binding to SARS-CoV-2 levels (Figure 4B). We also observed that Q70R modestly enhanced Tom70 binding in the SARS-CoV-2 T72I background, whereas R70Q further reduced Tom70 interaction in RaTG13. Also, we examined interactions of these mutants with hMTARC2. In line with the above results, we found that the RaTG13 Orf9b I72T mutation abolished MTARC2 binding, whereas MTARC2 binding was unaltered by R70Q mutation (Figure 4C). Similarly, the SARS-CoV-2 Orf9b T72I mutation gained interaction with MTARC2. These findings suggest that Orf9b residue 72 acts as

(F) Phylogenetic tree of 12 diverse coronavirus genomes, generated using a nucleotide alignment of N ORF. A 4aa region of Orf9b sequence of each virus is shown, with changes at residues 70 and 72 highlighted.
(G and H) CoIP of FLAG-tagged human Tom70 (G) or MTARC2 (H) with SARS-CoV-2 and RaTG13 Orf9b wild type and mutants in HEK293T cells.
Statistical significance was calculated relative to vector control using ANOVA with Tukey's test. ***$p < 0.001$, ****$p < 0.0001$.

Please cite this article in press as: Batra et al., Coronavirus protein interaction mapping in bat and human cells reveals network rewiring governing immune evasion and zoonotic potential, Cell Host & Microbe (2026), https://doi.org/10.1016/j.chom.2026.04.015

CellPress
OPEN ACCESS

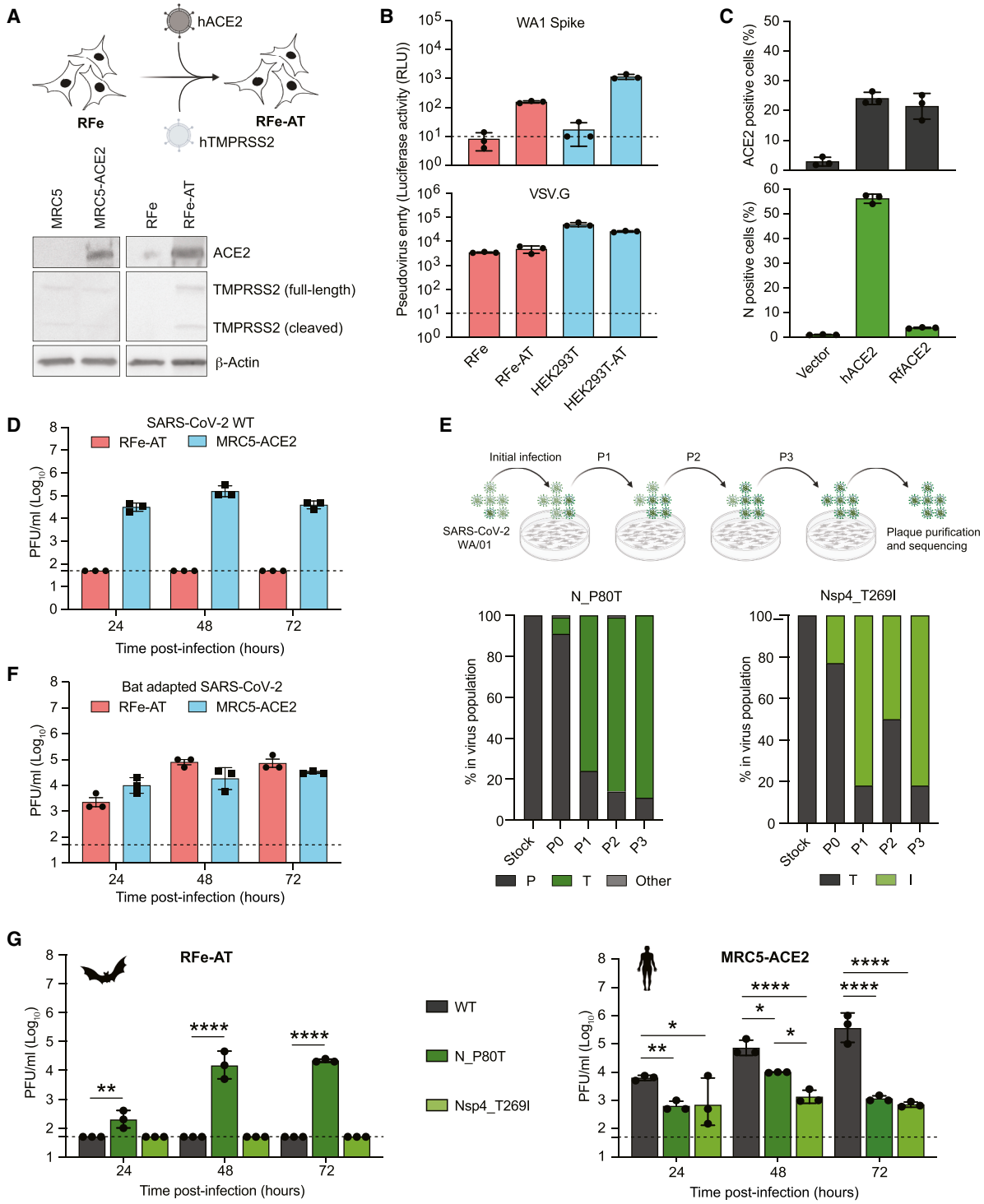

Figure 5. Establishment of a bat cell infection model through hACE2/hTMPRSS2 expression and SARS-CoV-2 adaptation

(A) Schematic illustrating the generation of the RFe-AT cell line by introducing hACE2 and hTMPRSS2 (top). Western blot analysis (bottom) shows expression of hACE2 and hTMPRSS2 (full length and cleaved forms).

(B) SARS-CoV-2 entry assays using pseudotyped HIV-1-based particles. Entry is shown as firefly luciferase relative luminescence units (RLUs).

(C) SARS-CoV-2 entry mediated by human (hACE2) or bat (RfACE2) in HEK293T cells (MOI = 1). The percentage of ACE2-positive (top) and N-positive (bottom) cells within the ACE2-positive population are shown.

(D) Replication kinetics of SARS-CoV-2 WA1 in RFe-AT and MRC5-ACE2 cells (MOI = 0.1) quantified by plaque assay at 24–72 hpi.

(legend continued on next page)

Please cite this article in press as: Batra et al., Coronavirus protein interaction mapping in bat and human cells reveals network rewiring governing immune evasion and zoonotic potential, Cell Host & Microbe (2026), https://doi.org/10.1016/j.chom.2026.04.015

a molecular switch of Orf9b interaction between Tom70 and MTARC2.

Given the role of SARS-CoV-2 Orf9b in suppressing innate immune response through Tom70,[28,29] we assessed how RaTG13 Orf9b affects downstream RNA sensing. We expressed SARS-CoV-2 or RaTG13 Orf9b, alongside vector control, in HEK293T cells expressing a Lucia reporter under the control of the interferon β (IFN-β)/ISG56 promoter and stimulated with poly(I:C). Consistent with our previous findings,[28] SARS-CoV-2 Orf9b significantly inhibited reporter activation compared with vector control, whereas RaTG13 Orf9b showed no significant difference (Figure 4D). Technical limitations prevented us from performing the same assay in RFe cells. Instead, we measured ISG induction by qPCR following Sendai virus (SeV) infection. Compared with vector control, SARS-CoV-2 Orf9b reduced Mx1 and OAS1 expression, whereas RaTG13 Orf9b had no significant effect (Figure 4E). These results correlate with reduced Tom70 binding of RaTG13 Orf9b, which may impair its function as an innate immune antagonist.

To better understand the evolutionary dynamics of Orf9b, we analyzed coronavirus genome sequences from human- and bat-derived virus sequences. Alignment of Orf9b protein sequences suggests that T72 is an ancestral residue in SARSr-CoVs: threonine is conserved across SARS-CoV-2 (HuSARS-CoV-2_Wu1), several closely related pangolin and bat viruses, and SARS-CoV (Figure 4F). Interestingly, the T72I substitution observed in RaTG13 also arose independently in multiple lineages, including more divergent clades (BtKY72 and BtBM48-31) and SARS-CoV-2 isolates (HuSARS-CoV-2_LC0020256); it was detected at low frequency in the human population throughout the pandemic (Figures S8B and S8C), consistent with previous estimates of its near-neutral fitness.[38] We also observed sequence variation at position 70, where arginine is present in RaTG13 and several bat and pangolin viruses, whereas glutamine is found in both SARS-CoV and SARS-CoV-2, as well as in their closest relatives. This observed pattern suggests that R70 was likely present in the common ancestor of RaTG13 and SARS-CoV-2, followed by reversion to Q in the SARS-CoV-2 lineage.

Together, these findings suggest that Orf9b position 72 is evolutionarily constrained, with T72 broadly conserved across SARSr-CoVs. To define its functional role, we introduced all possible single-nucleotide substitutions at codon 72 of SARS-CoV-2 or RaTG13 Orf9b and assessed host interactions by coIP (Figure 4G). Among these, T72P was the only additional SARS-CoV-2 mutant that markedly disrupted Tom70 binding, whereas T72A and T72S had minimal effects. Interestingly, we observed an opposite binding pattern with MTARC2, where T72P and T72A enhanced interaction, whereas T72S showed a similar binding (Figure 4H). These results suggest that residue 72 plays a differential role in modulating Orf9b interactions with distinct host targets, potentially through localized structural changes that selectively alter binding interfaces.

A single-nucleocapsid substitution supports productive SARS-CoV-2 infection in RFe-AT cells

To assess the relevance of our findings during infection, we established a bat cell model for SARS-CoV-2 replication. Parental RFe cells were non-permissive to virus infection. Therefore, we generated RFe cells stably expressing hACE2 and TMPRSS2 (RFe-AT) and confirmed expression by western blot (Figure 5A). Using HIV-1-based luciferase pseudoparticles with SARS-CoV-2 WA1 spike (Δ19),[39] we found that hACE2 and hTMPRSS2 expression was sufficient to overcome entry restriction in RFe cells. As expected, vesicular stomatitis virus (VSV)-G pseudotyped virus-like particles (VLPs) infected RFe and HEK293T cells independent of receptor expression (Figure 5B). These data suggest impaired spike interaction with endogenous RFe ACE2 or low ACE2 expression, consistent with reports from other bat cell lines.[40] RT-qPCR confirmed low endogenous ACE2 and TMPRSS2 transcript levels in RFe cells (Figure S9). To test whether limited RFe ACE2 levels contribute to this restriction, we overexpressed hemagglutinin (HA)-tagged greater horseshoe bat ACE2 (RfACE2) or hACE2 in HEK293T cells and quantified nucleocapsid-positive cells at 24 h post-infection (hpi) (Figure 5C). Transient expression of hACE2 supported efficient entry and replication, whereas RfACE2 did not. Together with prior reports,[41] these results indicate that RfACE2 fails to mediate SARS-CoV-2 entry, likely due to divergence at key spike RBD-interacting residues. To further assess RFe-AT permissiveness, we infected cells with SARS-CoV-2 WA1 for 72 h and monitored replication by plaque assay. Notably, no productive infection was detected in RFe-AT cells, whereas robust replication occurred in MRC5-ACE2 control cells (Figure 5D), indicating that RFe-AT cells are not permissive under these conditions. To assess whether viral adaptation might overcome this restriction, we performed high-MOI infection followed by three blind serial passages. Strikingly, whole-genome sequencing of viral RNA from each passage (Figure 5E) identified 3 nonsynonymous mutations: N_P80T (nucleocapsid), Nsp4_T269I, and S_R682W (spike). A plaque-purified virus carrying all three mutations replicated efficiently in RFe-AT cells, comparable with that in MRC5-ACE2 cells (Figure 5F). Since S_R682W is a known tissue culture adaptation[42] and all mutations have been detected at low frequency in human isolates,[43] we examined the contribution of N_P80T and Nsp4_T269I using reverse genetics. Recombinant viruses encoding each mutation individually showed that N_P80T alone was necessary and sufficient to enable productive replication in RFe-AT cells (Figure 5G). Both mutants replicated less efficiently than the wild type in MRC5-ACE2 cells, indicating host-specific adaptation to bat cells as opposed to compromising replication efficiency in human cells.

(E) Schematic overview of SARS-CoV-2 adaptation experiment in bat cells (top). Bar plots (bottom) show the frequency of specific missense mutations (N_P80T and Nsp4_T269I) in the viral population across passages.

(F) Replication kinetics of bat-adapted SARS-CoV-2 WA1 in RFe-AT and MRC5-ACE2 cells (MOI = 0.1) determined by plaque assay.

(G) Growth kinetics of recombinant SARS-CoV-2 WT, N_P80T, or Nsp4_T269I viruses in RFe-AT and MRC5-ACE2 (MOI = 0.1), measured by plaque assay. Dashed lines in (D), (F), and (G) indicate the plaque assay limit of detection (LOD; 50 plaque-forming unit [PFU]/mL). Values below LOD were plotted at this limit and excluded from statistics. Data are presented as mean ± SD from one biological replicate with three technical replicates ($n = 3$); statistical analysis was done using one-way ANOVA with Tukey's test. $^{*}p < 0.05$, $^{**}p < 0.005$, $^{****}p < 0.00005$.

Please cite this article in press as: Batra et al., Coronavirus protein interaction mapping in bat and human cells reveals network rewiring governing immune evasion and zoonotic potential, Cell Host & Microbe (2026), https://doi.org/10.1016/j.chom.2026.04.015

CellPress
OPEN ACCESS

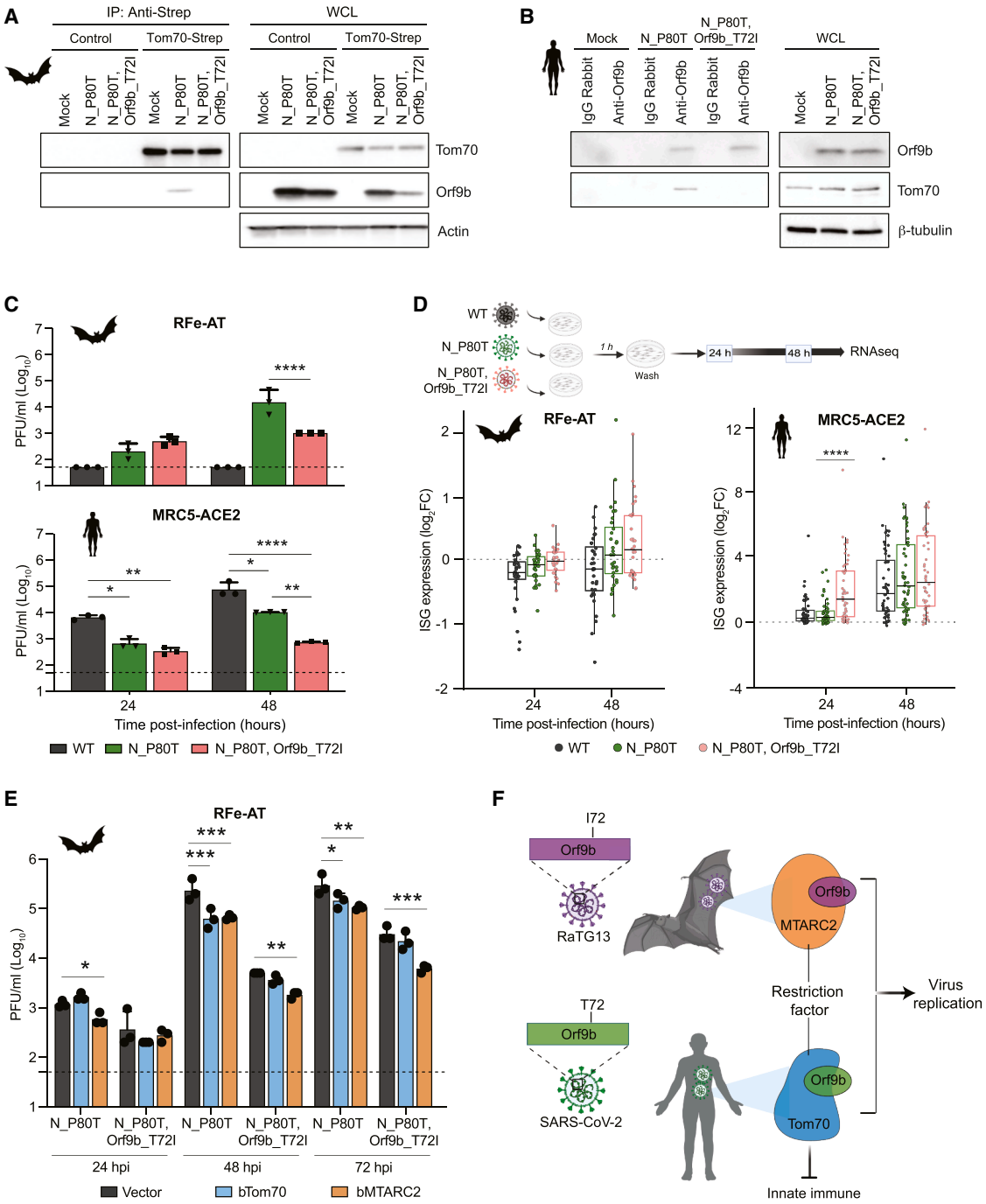

Figure 6. Orf9b T72I mutant lacking Tom70 binding modulates viral replication and immune signaling

(A) CoIP of endogenous 2xStrep-tagged Tom70 RFe-AT cells upon infection with SARS-CoV-2 N_P80T or N_P80T, Orf9b_T72I mutant viruses.

(B) CoIP of Orf9b in MRC5-ACE2 cells infected with SARS-CoV-2 N_P80T or N_P80T, Orf9b_T72I mutant viruses.

(C) Bar graphs showing viral titers in RFe-AT or MRC5-ACE2 cells infected with the indicated viruses.

(D) Schematic of the experimental design for bulk mRNA sequencing in RFe-AT and MRC5-ACE2 cells infected with indicated viruses (top). Boxplots (bottom) show log_2FC of ISGs relative to uninfected controls at each time point. Each dot represents an individual ISG; boxes indicate the median (center line) and interquartile range (upper and lower bounds).

(E) Bar graphs showing viral titers in RFe-AT cells stably expressing bTom70, bMTARC2, or vector control, following infection with indicated viruses.

(legend continued on next page)

Please cite this article in press as: Batra et al., Coronavirus protein interaction mapping in bat and human cells reveals network rewiring governing immune evasion and zoonotic potential, Cell Host & Microbe (2026), https://doi.org/10.1016/j.chom.2026.04.015

Loss of Tom70 binding by Orf9b enhances innate immune activation

Using the RFe-AT infection model, we examined the impact of Orf9b-Tom70/MTARC2 interactions on virus replication. We generated a bat-adapted SARS-CoV-2 N_P80T virus carrying Orf9b T72I mutation (rSARS-CoV-2 N_P80T, Orf9b_T72I) and assessed Orf9b-Tom70 binding during infection, compared with that of the rSARS-CoV-2 N_P80T virus. In RFe-AT cells expressing endogenously tagged Tom70-2xStrep, pull-down of Tom70 showed robust interaction with Orf9b in N_P80T-infected cells, but not with the T72I mutant (Figure 6A). Reciprocal coIP in infected MRC5-ACE2 cells using an anti-Orf9b antibody confirmed Tom70 binding to WT Orf9b but not to the T72I mutant (Figure 6B). Together, these coIP experiments demonstrate that T72-dependent Orf9b-Tom70 interaction occurs under physiological conditions in both bat and human cells.

Next, we compared the growth kinetics of rSARS-CoV-2 N_P80T, Orf9b_T72I with N_P80T and WT viruses in bat and human cells. As expected, the introduction of the Orf9b T72I mutation, which disrupts the Orf9b-Tom70 interaction, led to reduced viral titers at 48 hpi in both cells (Figure 6C). To further examine host innate immune responses, we performed bulk RNA-seq on cells infected with WT and mutant viruses at 24 and 48 hpi (Figure 6D). In MRC5-ACE2 cells, the Orf9b T72I mutant induced significantly stronger upregulation of ISGs at 24 hpi compared with that of WT and N_P80T viruses (Figures 6D, S10A, and S10B), indicating reduced suppression of host antiviral responses due to impaired Orf9b-Tom70 interaction. This was confirmed by qPCR analysis of a subset of ISGs (Figure S10C). This is consistent with our previous observations and other studies[28,29,44] showing Orf9b-mediated innate immune suppression through Tom70. The ISG response was markedly less pronounced in RFe-AT cells (Figure 6D), suggesting that cell-intrinsic differences, such as dampened or delayed innate immune activation contribute to reduced ISG induction observed in bat cells. In RFe-AT cells, ISGs were modestly upregulated in response to infection, with relatively small differences between N_P80T and N_P80T, Orf9b_T72I (Figures 6D and S10C; Table S5).

To assess the functional impact of Tom70 and MTARC2 on SARS-CoV-2 replication in bat cells, we generated RFe-AT cells stably overexpressing bat MTARC2, Tom70, or vector control (Figure S10D). Upon infection with SARS-CoV-2 N_P80T virus, Tom70- or MTARC2-overexpressing cells showed a modest reduction in viral titers compared with vector control (Figure 6E), indicating restriction of viral replication to some extent. Notably, MTARC2 conferred stronger restriction at 72 hpi with N_P80T, Orf9b_T72I mutant virus, which shows enhanced binding to MTARC2. These findings suggest a role of MTARC2-Orf9b interaction in restricting viral replication in bat cells. In contrast, Tom70 overexpression did not result in a significant difference in viral titers compared with control following infection with N_P80T, Orf9b_T72I mutant virus. To assess whether MTARC2 broadly restricts RNA virus replication, we evaluated its effect on VSV and influenza A virus strains (A/WSN/1933 and A/Puerto Rico/8/1934) in RFe-AT cells. MTARC2 did not alter replication of VSV or influenza A viruses across multiple MOIs (Figure S10E), indicating a coronavirus-specific antiviral role.

Our findings confirm previous studies, which showed that SARS-CoV-2 Orf9b suppresses innate immunity via Tom70 to promote replication (Figure 6F). In contrast, RaTG13 Orf9b (I72) preferentially interacts with a different mitochondrial protein, MTARC2, in bat cells, where this interaction restricts viral replication. Introducing the T72I mutation in SARS-CoV-2 Orf9b disrupts Tom70 binding while enhancing MTARC2 interaction, leading to impaired immune evasion and attenuated replication in both bat and human cells. These results highlight a potential evolutionary trade-off in viral adaptation, where Orf9b switches host targets to modulate replication and immune evasion in a species-specific manner.

DISCUSSION

The frequency of zoonotic spillovers of bat-borne viruses causing severe diseases in humans[45] and other animals[46] underscores the need for bat-derived cellular models to investigate host-virus dynamics and to better understand the mechanisms that enable bats to function as efficient viral reservoirs. In this study, we describe the generation of an immortalized lung fibroblast cell line from the greater horseshoe bat, a species within the *Rhinolophus* genus known to harbor SARS-like coronaviruses with pandemic potential.

To enable mechanistic and comparative infection studies across human and bat cells, we created 2 additional resources. First, we rendered our RFe cell line susceptible to SARS-CoV-2 infection by overexpression of hACE2 and TMPRSS2. hACE2 was required for viral entry, consistent with previous findings that SARS-CoV-2 cannot use RFe ACE2,[41] or ACE2 orthologs from other bat species.[9] However, no spread of infection was observed, indicating that viral adaptation is required for efficient replication in bat cells and suggesting the presence of additional host-specific barriers beyond receptor incompatibility. We identified a single mutation in the viral nucleocapsid (N_P80T) that enables productive replication of SARS-CoV-2 in greater horseshoe bat cells. Notably, this mutation is synonymous with Orf9b residue V76. Although the precise mechanism that licenses SARS-CoV-2 replication remains to be elucidated, this mutation may influence nucleocapsid-host interactions rather than intrinsic within-virus functions such as RNA binding or phase separation, which would be expected to have similar effects across hosts. For instance, N_P80T may modulate interactions with bat-specific immune sensors or stress granule components—processes known to impact viral replication and innate immune evasion.[27,47] SARSr-CoVs detected in horseshoe bats, including RaTG13, differ in several amino acids near position 80 in the N protein. It might be

(F) Model illustrating Orf9b host adaptation. RaTG13 Orf9b (I72) preferentially interacts with MTARC2 in bat cells, restricting viral replication, whereas SARS-CoV-2 Orf9b (T72) binds Tom70 in human cells to suppress innate immune signaling.

Dashed lines in (C) and (E) indicate the limit of detection (LOD; 50 PFU/mL). Values below LOD were plotted at this limit and excluded from statistics. Data are presented as mean ± SD from one biological replicate with three technical replicates ($n = 3$); statistical analysis was done using one-way ANOVA with Tukey's test. $^{*}p < 0.05$, $^{**}p < 0.005$, $^{***}p < 0.0005$, and $^{****}p < 0.00005$.

Please cite this article in press as: Batra et al., Coronavirus protein interaction mapping in bat and human cells reveals network rewiring governing immune evasion and zoonotic potential, Cell Host & Microbe (2026), https://doi.org/10.1016/j.chom.2026.04.015

possible that polymorphisms in the amino terminal RNA-binding domain of the N protein are responsible for specific adaptations to different mammalian species, including bats. Ongoing work to characterize the underlying mechanisms is likely to reveal species-specific restriction or dependency factors and inform risk assessments for the emergence potential of other bat-derived sarbecoviruses.

Although bat coronaviruses are thought to primarily replicate in intestinal epithelial cells in their natural hosts, well-characterized bat intestinal cell lines are currently lacking, and the available organoid systems[48–51] are not readily scalable or genetically tractable for systematic proteomic and functional studies. To enable these studies, we therefore generated immortalized bat lung fibroblast cell lines as the methods to generate these cell types are widely used. Importantly, SARS-CoV-2 can infect ACE2-expressing human fibroblasts,[52] supporting the suitability of this model to study coronavirus replication and virus-host dynamics in a bat cellular background. Through proteomics-based comparative interactome mapping in human and bat cells, we identified shared and distinct PPIs for SARS-CoV-2 and its close bat coronavirus relative, RaTG13. Both viruses target core cellular processes, including RNA metabolism, protein trafficking, and innate immune regulation. We identified a conserved interaction between Orf3a and HOPS complex in both viruses, consistent with a previous report that both SARS-CoV-2 and RaTG13 Orf3a interfere with autophagy.[53,54] Our study also revealed virus- and host-specific interactions, illustrating how subtle variations in viral proteins can lead to distinct molecular interactions and host responses.

We identified a bat-specific RaTG13 Nsp12-ISG15 interaction; notably, bat ISG15 carries key residue changes across *Rhinolophus* species and exhibits stronger anti-SARS-CoV-2 activity than human ISG15.[55] Despite high sequence similarity between SARS-CoV-2 and RaTG13, we observed limited overlap in their interactomes within the same host, suggesting functional divergence among closely related sarbecoviruses. Understanding this divergence may reveal species-specific vulnerabilities and inform the development of targeted therapeutic strategies.

Finally, we described how subtle differences in Orf9b can reshape virus-host interactions across species. SARS-CoV-2 Orf9b targets Tom70 to suppress innate immunity across host species, consistent with its role in mitochondrial immune modulation.[18,28] In contrast, RaTG13 Orf9b preferentially binds MTARC2 in bat cells. MTARC2 regulates mitochondrial redox balance and may modulate antiviral signaling pathways by influencing reactive oxygen species (ROS) levels, inflammation, and interferon responses.[31,56,57] This interaction, leading to an MTARC2-mediated reduction in viral replication, may reflect Orf9b's adaptation to the bat immune landscape, which is characterized by viral tolerance and reduced immunopathology. The functional relevance of these interactions is highlighted by our finding that a single substitution (T72I) in Orf9b disrupts Tom70 binding while enhancing MTARC2 interaction. When introduced into the bat-adapted virus, it attenuated replication in both bat and human cells, correlating with stronger innate responses in human cells and modest ISG induction in bat cells. The reduced replication of the T72I mutant in bat cells may be driven in part by MTARC2-specific functional effects, including modulation of metabolic or redox pathways, in addition to modest upregulation of ISG response. Further, MTARC2 overexpression restricts SARS-CoV-2 replication in bat cells, suggesting a coronavirus-specific antiviral role. Although MTARC2 has no known antiviral role in humans, its interaction with RaTG13 suggests that mitochondrial or metabolic regulators may influence virus fitness in bat reservoirs.

Interaction with MTARC2 is a derived trait observed in RaTG13 and a few other sarbecoviruses, gained at the expense of ancestral Tom70 interaction, illustrating the importance of MTARC2 as a previously unrecognized restriction factor, at least in bat cells. Interestingly, T72I is a synonymous mutation in the overlapping N ORF, whereas all other substitutions result in nonsynonymous changes. Despite the neutrality in N ORF, T72I remains rare in human SARS-CoV-2 isolates, conceivably due to impaired Tom70-mediated immune suppression. This highlights a dual evolutionary constraint at Orf9b position 72 and underscores the importance of viral accessory protein and host protein interactions in shaping viral fitness, immune modulation, and host adaptation, similar to poxviruses in which variations in accessory protein repertoires are related to host range and virulence.[58]

More broadly, our study highlights the utility of systematic host-virus interaction mapping across species as a powerful approach for dissecting the molecular underpinnings of host adaptation, immune evasion, and zoonotic emergence. Our findings underscore the evolutionary flexibility of accessory proteins such as Orf9b in fine-tuning species-specific host interactions. The functional divergence between Orf9b orthologs in their ability to suppress host defenses may shape viral fitness and spillover potential. Future work defining the mechanisms and structures of bat-specific interactions, including MTARC2 and flotillins, will provide insight into evolutionary constraints governing these interactions. Systematic, cross-species interactome mapping combined with functional infection models in reservoir hosts offers a powerful framework for identifying molecular signatures predictive of zoonotic emergence. Expanding these approaches across diverse bat species and viral families will be essential for future pandemic preparedness.

RESOURCE AVAILABILITY

Lead contact

Requests for further information and resources should be directed to and will be fulfilled by the lead contact, Nevan J. Krogan (nevan.krogan@ucsf.edu).

Materials availability

All the reagents generated in this study are available from the lead contact.

Data and code availability

- Raw files for all the proteomics and RNA-seq data have been deposited to PRIDE[59] (project ID: PRIDE: PXD065873) and GEO (accession number: GSE302357), respectively. They are publicly available as of the date of publication.
- This paper does not report the original code. All software tools used in this paper are publicly available and listed in the key resources table.
- Any additional information required to reanalyze the data reported in this paper is available from the lead contact upon request.

ACKNOWLEDGMENTS

We would like to thank John Huddleston and Katie Kistler for useful discussions on SARS-CoV2 mutation frequencies. We also thank Richard Cadagan for excellent technical assistance and Dr. Randy Albrecht for support with the BSL3 facility and procedures at the ISMMS. We thank Dr. Arturo Marin for his previous bioinformatics analysis for this work, conducted as part of his postdoctoral fellowship from December 1, 2020, to December 14, 2023, at the Icahn School of Medicine at Mount Sinai. We thank Delini Samarasignhe for her assistance in collecting cell pellets for AP-MS studies in bat cells. This research was funded by grants from the National Institutes of Health (U19AI135990 to N.J.K., M.O., and J.B.; U19AI135972 to A.G.-S., N.J.K., and J.B.; U54AI170792 to H.S.M.; R01AI170596 to J.R.J.; R35GM160071 to M.B.; T32GM145388 to D.M.W). H.S.M. is an Investigator of the Howard Hughes Medical Institute. I.P.C. was supported by NIH/NIAID (F31AI164671-01). M.O. received support from the James B. Pendleton Charitable Trust, Roddenberry Foundation, P. and E. Taft, and the Gladstone Institutes. M.O. thanks Fast Grants and the Innovative Genomics Institute for their support. M.O. is a Biohub, San Francisco Investigator. Experiments performed in the N.J. laboratory were funded by ANR EmerCoV AAP CE35. Research reported in this publication in the BSL3 facility was supported by the NIAID/NIH under award number G20AI174733 (R.A. Albrecht). This work was supported in part through the computational and data resources and staff expertise provided by Scientific Computing and Data at the Icahn School of Medicine at Mount Sinai and supported by the Clinical and Translational Science Awards (CTSA) grant UL1TR004419 from the National Center for Advancing Translational Sciences. Research reported in this publication was also supported by the Office of Research Infrastructure of the National Institutes of Health under award number S10OD026880 and S10OD030463. The content is solely the responsibility of the authors and does not necessarily represent the official views of the National Institutes of Health. R.K.S. is supported by the NIH Division of Intramural Research. This research was supported in part by the Intramural Research Program of the National Institutes of Health (NIH). The contributions of the NIH author were made as a part of their official duties as NIH federal employees, are in compliance with the agency policy requirements, and are considered Works of the United States Government. However, the findings and conclusions presented in this paper are those of the author and do not necessarily reflect the views of the NIH or the U.S. Department of Health and Human Services.

AUTHOR CONTRIBUTIONS

The following authors designed and conceptualized the study: N.J.K., A.G.-S., L.M., J.B., H.S.M., and M.R. The following authors performed experiments or data acquisition: J.B., M.R., C.Y., R.A., D.A., S.V., H.P., S. Malpotra, A.C., T.K., M.D.S., R.B., J.M.M., V.C., A.R., I.M., S.A., C.M.-R., I.C.V., K.F., F.V.-L., A.B., A.D., S. Maji, M.M., H.F., I.P.C., C.J.S.F., S.G., R.K.S., B.B., C.I., T.Y.T., and J.J. The following authors conducted data processing or analysis: J.B., M.R., Y.Z., M.G., B.J.P., I.P.C., J.M.Y., D.M.W., I.E., D.T.-C., R.F., C.D., T.Y.T., M.E., Z.K., and I.M. The following authors supervised research: N.J.K., A.G.-S., L.M., L.M.-S., M.O., D.L.S., H.v.B., B.J.P., M.B., T.H., H.S.M., J.S.F., K.A.V., R.M.S., N.J., K.O., J.R.J., and L.Z.-A. The following authors drafted the original manuscript: J.B., M.R., and M.E. All authors edited the manuscript.

DECLARATION OF INTERESTS

N.J.K. has monetary and/or stock compensation with the following companies: GEn1E Lifesciences, Maze Therapeutics, Mreza Therapeutics, Rezo Therapeutics, and Tenaya Therapeutics. The A.G.-S. laboratory has received research support from Avimex, Dynavax, Pharmamar, 7Hills Pharma, ImmunityBio, and Accurius, outside of the reported work. A.G.-S. has consulting agreements for the following companies involving cash and/or stock: Castlevax, Amovir, Vivaldi Biosciences, Contrafect, 7Hills Pharma, Avimex, Pagoda, Accurius, Esperovax, Applied Biological Laboratories, Pharmamar, CureLab Oncology, CureLab Veterinary, Synairgen, Paratus, Pfizer, Virofend, and Prosetta, outside of the reported work. A.G.-S. has been an invited speaker in meeting events organized by Seqirus, Janssen, Abbott, Astrazeneca, and Novavax. A.G.-S. is inventor on patents and patent applications on the use of antivirals and vaccines for the treatment and prevention of virus infections and cancer, owned by the Icahn School of Medicine at Mount Sinai, New York, outside of the reported work.

DECLARATION OF GENERATIVE AI AND AI-ASSISTED TECHNOLOGIES IN THE WRITING PROCESS

During the preparation of this manuscript, the authors used ChatGPT to rephrase or shorten portions of the text. All content generated with the assistance of this tool was subsequently reviewed and edited as needed by the authors, who take full responsibility for the content of the publication.

STAR★METHODS

Detailed methods are provided in the online version of this paper and include the following:

- KEY RESOURCES TABLE
- EXPERIMENTAL MODEL AND SUBJECT DETAILS
  - Capturing and sampling of greater horseshoe bats
  - Establishment of bat primary lung fibroblasts
  - Immortalization of bat primary lung fibroblasts
  - Generation of greater horseshoe bat lung fibroblasts stably expressing human ACE2 and TMPRSS2
  - Generation of greater horseshoe bat lung fibroblasts stably expressing bat Tom70 or MTARC2
  - Cell culture
  - Viruses and infections
- METHOD DETAILS
  - Virus stock sequencing
  - SARS-CoV-2 adaptation to RFe-AT lung fibroblasts
  - Generation of HIV-based pseudotyped particles
  - Pseudotyped virus entry assay
  - Infection of HEK293T cells overexpressing ACE2 orthologs with SARS-CoV-2 WA/01 virus
  - Immunofluorescence labeling of cells with α-tubulin antibody
  - Species origin characterization of RFe with RNAseq
  - RaTG13 annotation and plasmid cloning
  - Transfection in HEK293T cells for AP-MS studies
  - Transduction in RFe cells for AP-MS studies
  - Sample preparation for AP-MS studies
  - MS data acquisition and peptide search
  - Ortholog mapping of RFe proteins and percent identity
  - High-confidence protein interaction scoring and DIS analysis
  - Network generation and visualization
  - Analysis of *Rhinolophus ferrumequinum* - *Rhinolophus affinis* orthology
  - Deep proteome profiling
  - Orf9b PPI and MSstats analysis
  - Network propagation
  - Co-immunoprecipitation assays
  - Gaussia Princeps Protein Complementation Assay (GPCA)
  - Innate immune sensing assay in HEK293T cells
  - Endotagging of Tom70 in RFe-AT cells and co-IP assays upon infection
  - Co-IP assays with endogenous Tom70 in MRC5-ACE2 cells upon infection
  - Quantitative RT-PCR analysis
  - RNAseq analysis
  - RaTG13 Orf9b-hTom70 structure modeling
  - Orf9b evolutionary studies
  - SARS-CoV-2 mutation frequency
- QUANTIFICATION AND STATISTICAL ANALYSIS

SUPPLEMENTAL INFORMATION

Supplemental information can be found online at https://doi.org/10.1016/j.chom.2026.04.015.

Received: July 23, 2025
Revised: February 27, 2026
Accepted: April 15, 2026

REFERENCES

1. World Health Organization (2026). COVID-19 deaths datadot. https://data.who.int/dashboards/covid19/deaths?n=o.
2. Temmam, S., Vongphayloth, K., Baquero, E., Munier, S., Bonomi, M., Regnault, B., Douangboubpha, B., Karami, Y., Chrétien, D., Sanamxay, D., et al. (2022). Bat coronaviruses related to SARS-CoV-2 and infectious for human cells. Nature *604*, 330–336. https://doi.org/10.1038/s41586-022-04532-4.
3. Xiao, K., Zhai, J., Feng, Y., Zhou, N., Zhang, X., Zou, J.-J., Li, N., Guo, Y., Li, X., Shen, X., et al. (2020). Isolation of SARS-CoV-2-related coronavirus from Malayan pangolins. Nature *583*, 286–289. https://doi.org/10.1038/s41586-020-2313-x.
4. Li, W., Shi, Z., Yu, M., Ren, W., Smith, C., Epstein, J.H., Wang, H., Crameri, G., Hu, Z., Zhang, H., et al. (2005). Bats are natural reservoirs of SARS-like coronaviruses. Science *310*, 676–679. https://doi.org/10.1126/science.1118391.
5. Zhou, P., Yang, X.-L., Wang, X.-G., Hu, B., Zhang, L., Zhang, W., Si, H.-R., Zhu, Y., Li, B., Huang, C.-L., et al. (2020). A pneumonia outbreak associated with a new coronavirus of probable bat origin. Nature *579*, 270–273. https://doi.org/10.1038/s41586-020-2012-7.
6. Aicher, S.-M., Streicher, F., Chazal, M., Planas, D., Luo, D., Buchrieser, J., Nemcova, M., Seidlova, V., Zukal, J., Serra-Cobo, J., et al. (2022). Species-specific molecular barriers to SARS-CoV-2 replication in bat cells. J. Virol. *96*, e0060822. https://doi.org/10.1128/jvi.00608-22.
7. Zhou, H., Ji, J., Chen, X., Bi, Y., Li, J., Wang, Q., Hu, T., Song, H., Zhao, R., Chen, Y., et al. (2021). Identification of novel bat coronaviruses sheds light on the evolutionary origins of SARS-CoV-2 and related viruses. Cell *184*, 4380–4391.e14. https://doi.org/10.1016/j.cell.2021.06.008.
8. Bisht, P., Gallagher, M.D., Barrasa, M.I., Boucau, J., Harding, A., Déjosez, M., Godoy-Parejo, C., Bisher, M.E., de Nola, G., Lytton-Jean, A.K.R., et al. (2024). Abortive infection of bat fibroblasts with SARS-CoV-2. Proc. Natl. Acad. Sci. USA *121*, e2406773121. https://doi.org/10.1073/pnas.2406773121.
9. Baid, K., Shrivastava, S., Luc, J., Richard, D., Aguiar, J.A., Machado, Y., Aicher, S.-M., Siwak, K.C., LeBlanc, E.V., Khatooni, Z., et al. (2025). Early innate immune response and evolution of a SARS-CoV-2 furin cleavage site inactive variant in bat cells. Cell Rep. *44*, 115929. https://doi.org/10.1016/j.celrep.2025.115929.
10. Chen, Z., Wang, C., Feng, X., Nie, L., Tang, M., Zhang, H., Xiong, Y., Swisher, S.K., Srivastava, M., and Chen, J. (2021). Interactomes of SARS-CoV-2 and human coronaviruses reveal host factors potentially affecting pathogenesis. EMBO J. *40*, e107776. https://doi.org/10.15252/embj.2021107776.
11. Zhou, Y., Liu, Y., Gupta, S., Paramo, M.I., Hou, Y., Mao, C., Luo, Y., Judd, J., Wierbowski, S., Bertolotti, M., et al. (2023). A comprehensive SARS-CoV-2-human protein-protein interactome reveals COVID-19 pathobiology and potential host therapeutic targets. Nat. Biotechnol. *41*, 128–139. https://doi.org/10.1038/s41587-022-01474-0.
12. Gordon, D.E., Jang, G.M., Bouhaddou, M., Xu, J., Obernier, K., White, K.M., O'Meara, M.J., Rezelj, V.V., Guo, J.Z., Swaney, D.L., et al. (2020). A SARS-CoV-2 protein interaction map reveals targets for drug repurposing. Nature *583*, 459–468. https://doi.org/10.1038/s41586-020-2286-9.
13. Castresana, J. (2001). Cytochrome b phylogeny and the taxonomy of great apes and mammals. Mol. Biol. Evol. *18*, 465–471. https://doi.org/10.1093/oxfordjournals.molbev.a003825.
14. Teo, G., Liu, G., Zhang, J., Nesvizhskii, A.I., Gingras, A.-C., and Choi, H. (2014). SAINTexpress: improvements and additional features in Significance Analysis of INTeractome software. J. Proteom. *100*, 37–43. https://doi.org/10.1016/j.jprot.2013.10.023.
15. Verschueren, E., Von Dollen, J., Cimermancic, P., Gulbahce, N., Sali, A., and Krogan, N.J. (2015). Scoring large-scale Affinity Purification Mass Spectrometry datasets with MiST. Curr. Protoc. Bioinform. *49*, 8.19.1–8.19.16. https://doi.org/10.1002/0471250953.bi0819s49.
16. Ficarelli, M., Neil, S.J.D., and Swanson, C.M. (2021). Targeted restriction of viral gene expression and replication by the ZAP antiviral system. Annu. Rev. Virol. *8*, 265–283. https://doi.org/10.1146/annurev-virology-091919-104213.
17. Kerns, J.A., Emerman, M., and Malik, H.S. (2008). Positive selection and increased antiviral activity associated with the PARP-containing isoform of human zinc-finger antiviral protein. PLoS Genet. *4*, e21. https://doi.org/10.1371/journal.pgen.0040021.
18. Gordon, D.E., Hiatt, J., Bouhaddou, M., Rezelj, V.V., Ulferts, S., Braberg, H., Jureka, A.S., Obernier, K., Guo, J.Z., Batra, J., et al. (2020). Comparative host-coronavirus protein interaction networks reveal pan-viral disease mechanisms. Science *370*, eabe9403. https://doi.org/10.1126/science.abe9403.
19. Liu, P., Wang, X., Sun, Y., Zhao, H., Cheng, F., Wang, J., Yang, F., Hu, J., Zhang, H., Wang, C.-C., et al. (2022). SARS-CoV-2 ORF8 reshapes the ER through forming mixed disulfides with ER oxidoreductases. Redox Biol. *54*, 102388. https://doi.org/10.1016/j.redox.2022.102388.
20. Giurgiu, M., Reinhard, J., Brauner, B., Dunger-Kaltenbach, I., Fobo, G., Frishman, G., Montrone, C., and Ruepp, A. (2019). CORUM: the comprehensive resource of mammalian protein complexes-2019. Nucleic Acids Res. *47*, D559–D563. https://doi.org/10.1093/nar/gky973.
21. Ashburner, M., Ball, C.A., Blake, J.A., Botstein, D., Butler, H., Cherry, J.M., Davis, A.P., Dolinski, K., Dwight, S.S., Eppig, J.T., et al. (2000). Gene Ontology: Tool for the Unification of Biology. Nature Genetics *25*, 25–29. https://doi.org/10.1038/75556.
22. (2026). Gene Ontology Consortium. The Gene Ontology knowledgebase in 2026. Nucleic. Acids Res. *54* (D1), D1779–D1792. https://doi.org/10.1093/nar/gkaf1292.
23. Álvarez, E., Falqui, M., Sin, L., McGrail, J.P., Perdiguero, B., Coloma, R., Marcos-Villar, L., Tárrega, C., Esteban, M., Gómez, C.E., et al. (2024). Unveiling the multifaceted roles of ISG15: From immunomodulation to therapeutic frontiers. Vaccines (Basel) *12*, 153. https://doi.org/10.3390/vaccines12020153.
24. Zhu, X., Song, Z., Zhang, S., Nanda, A., and Li, G. (2014). CD147: a novel modulator of inflammatory and immune disorders. Curr. Med. Chem. *21*, 2138–2145. https://doi.org/10.2174/0929867321666131227163352.
25. Huang, W., Wang, L., Huang, Z., Sun, Z., and Zheng, B. (2024). Peroxiredoxin 3 has a crucial role in the macrophage polarization by regulating mitochondrial homeostasis. Respir. Res. *25*, 110. https://doi.org/10.1186/s12931-024-02739-9.
26. Plebanek, M.P., Bhaumik, D., Bryce, P.J., and Thaxton, C.S. (2018). Scavenger receptor type B1 and lipoprotein nanoparticle inhibit myeloid-derived suppressor cells. Mol. Cancer Ther. *17*, 686–697. https://doi.org/10.1158/1535-7163.MCT-17-0981.
27. Liu, H., Bai, Y., Zhang, X., Gao, T., Liu, Y., Li, E., Wang, X., Cao, Z., Zhu, L., Dong, Q., et al. (2022). SARS-CoV-2 N protein antagonizes stress granule assembly and IFN production by interacting with G3BPs to facilitate viral replication. J. Virol. *96*, e0041222. https://doi.org/10.1128/jvi.00412-22.
28. Thorne, L.G., Bouhaddou, M., Reuschl, A.-K., Zuliani-Alvarez, L., Polacco, B., Pelin, A., Batra, J., Whelan, M.V.X., Hosmillo, M., Fossati, A., et al. (2022). Evolution of enhanced innate immune evasion by SARS-CoV-2. Nature *602*, 487–495. https://doi.org/10.1038/s41586-021-04352-y.
29. Jiang, H.-W., Zhang, H.-N., Meng, Q.-F., Xie, J., Li, Y., Chen, H., Zheng, Y.-X., Wang, X.-N., Qi, H., Zhang, J., et al. (2020). SARS-CoV-2 Orf9b suppresses type I interferon responses by targeting TOM70. Cell. Mol. Immunol. *17*, 998–1000. https://doi.org/10.1038/s41423-020-0514-8.

30. Rixen, S., Havemeyer, A., Tyl-Bielicka, A., Pysniak, K., Gajewska, M., Kulecka, M., Ostrowski, J., Mikula, M., and Clement, B. (2019). Mitochondrial amidoxime-reducing component 2 (MARC2) has a significant role in N-reductive activity and energy metabolism. J. Biol. Chem. *294*, 17593–17602. https://doi.org/10.1074/jbc.RA119.007606.

31. Rixen, S., Indorf, P.M., Kubitza, C., Struwe, M.A., Klopp, C., Scheidig, A.J., Kunze, T., and Clement, B. (2023). Reduction of hydrogen peroxide by human mitochondrial amidoxime reducing component enzymes. Molecules *28*, 6384. https://doi.org/10.3390/molecules28176384.

32. Cassonnet, P., Rolloy, C., Neveu, G., Vidalain, P.-O., Chantier, T., Pellet, J., Jones, L., Muller, M., Demeret, C., Gaud, G., et al. (2011). Benchmarking a luciferase complementation assay for detecting protein complexes. Nat. Methods *8*, 990–992. https://doi.org/10.1038/nmeth.1773.

33. Vincentelli, R., Luck, K., Poirson, J., Polanowska, J., Abdat, J., Blémont, M., Turchetto, J., Iv, F., Ricquier, K., Straub, M.-L., et al. (2015). Quantifying domain-ligand affinities and specificities by high-throughput holdup assay. Nat. Methods *12*, 787–793. https://doi.org/10.1038/nmeth.3438.

34. Hu, B., Zeng, L.-P., Yang, X.-L., Ge, X.-Y., Zhang, W., Li, B., Xie, J.-Z., Shen, X.-R., Zhang, Y.-Z., Wang, N., et al. (2017). Discovery of a rich gene pool of bat SARS-related coronaviruses provides new insights into the origin of SARS coronavirus. PLoS Pathog. *13*, e1006698. https://doi.org/10.1371/journal.ppat.1006698.

35. Gao, X., Zhu, K., Qin, B., Olieric, V., Wang, M., and Cui, S. (2021). Crystal structure of SARS-CoV-2 Orf9b in complex with human TOM70 suggests unusual virus-host interactions. Nat. Commun. *12*, 2843. https://doi.org/10.1038/s41467-021-23118-8.

36. Jin, X., Sun, X., Chai, Y., Bai, Y., Li, Y., Hao, T., Qi, J., Song, H., Wong, C.C.L., and Gao, G.F. (2023). Structural characterization of SARS-CoV-2 dimeric ORF9b reveals potential fold-switching trigger mechanism. Sci. China Life Sci. *66*, 152–164. https://doi.org/10.1007/s11427-022-2168-8.

37. Drozdetskiy, A., Cole, C., Procter, J., and Barton, G.J. (2015). JPred4: a protein secondary structure prediction server. Nucleic Acids Res. *43*, W389–W394. https://doi.org/10.1093/nar/gkv332.

38. Bloom, J.D., and Neher, R.A. (2023). Fitness effects of mutations to SARS-CoV-2 proteins. Virus Evol. https://doi.org/10.1093/ve/vead055.

39. Schmidt, F., Weisblum, Y., Muecksch, F., Hoffmann, H.-H., Michailidis, E., Lorenzi, J.C.C., Mendoza, P., Rutkowska, M., Bednarski, E., Gaebler, C., et al. (2020). Measuring SARS-CoV-2 neutralizing antibody activity using pseudotyped and chimeric viruses. J. Exp. Med. *217*, e20201181. https://doi.org/10.1084/jem.20201181.

40. Letko, M., Marzi, A., and Munster, V. (2020). Functional assessment of cell entry and receptor usage for SARS-CoV-2 and other lineage B betacoronaviruses. Nat. Microbiol. *5*, 562–569. https://doi.org/10.1038/s41564-020-0688-y.

41. Yan, H., Jiao, H., Liu, Q., Zhang, Z., Xiong, Q., Wang, B.-J., Wang, X., Guo, M., Wang, L.-F., Lan, K., et al. (2021). ACE2 receptor usage reveals variation in susceptibility to SARS-CoV and SARS-CoV-2 infection among bat species. Nat. Ecol. Evol. *5*, 600–608. https://doi.org/10.1038/s41559-021-01407-1.

42. Ogando, N.S., Dalebout, T.J., Zevenhoven-Dobbe, J.C., Limpens, R.W.A.L., van der Meer, Y., Caly, L., Druce, J., de Vries, J.J.C., Kikkert, M., Bárcena, M., et al. (2020). SARS-coronavirus-2 replication in Vero E6 cells: replication kinetics, rapid adaptation and cytopathology. J. Gen. Virol. *101*, 925–940. https://doi.org/10.1099/jgv.0.001453.

43. Nextstrain., auspice. (2026). https://nextstrain.org/ncov/gisaid/global/6m?c=gt-N_80.

44. Ayinde, K.S., Pinheiro, G.M.S., and Ramos, C.H.I. (2022). Binding of SARS-CoV-2 protein ORF9b to mitochondrial translocase TOM70 prevents its interaction with chaperone HSP90. Biochimie *200*, 99–106. https://doi.org/10.1016/j.biochi.2022.05.016.

45. Wang, L.-F., and Anderson, D.E. (2019). Viruses in bats and potential spillover to animals and humans. Curr. Opin. Virol. *34*, 79–89. https://doi.org/10.1016/j.coviro.2018.12.007.

46. Letko, M., Seifert, S.N., Olival, K.J., Plowright, R.K., and Munster, V.J. (2020). Bat-borne virus diversity, spillover and emergence. Nat. Rev. Microbiol. *18*, 461–471. https://doi.org/10.1038/s41579-020-0394-z.

47. Cai, S., Zhang, C., Zhuang, Z., Zhang, S., Ma, L., Yang, S., Zhou, T., Wang, Z., Xie, W., Jin, S., et al. (2023). Phase-separated nucleocapsid protein of SARS-CoV-2 suppresses cGAS-DNA recognition by disrupting cGAS-G3BP1 complex. Signal Transduct. Target. Ther. *8*, 170. https://doi.org/10.1038/s41392-023-01420-9.

48. Kim, H., Heo, S.-Y., Kim, Y.-I., Park, D., N, M.P.A., Hwang, S., Lee, Y.-K., Jang, H., Ahn, J.-W., Ha, J., et al. (2025). Diverse bat organoids provide pathophysiological models for zoonotic viruses. Science *388*, 756–762. https://doi.org/10.1126/science.adt1438.

49. Liu, X., Li, C., Wan, Z., Chiu, M.C., Huang, J., Yu, Y., Zhu, L., Cai, J.-P., Rong, L., Song, Y.-Q., et al. (2022). Analogous comparison unravels heightened antiviral defense and boosted viral infection upon immunosuppression in bat organoids. Signal Transduct. Target. Ther. *7*, 392. https://doi.org/10.1038/s41392-022-01247-w.

50. Elbadawy, M., Saito, N., Kato, Y., Hayashi, K., Abugomaa, A., Kobayashi, M., Yoshida, T., Shibutani, M., Kaneda, M., Yamawaki, H., et al. (2025). Establishment of a bat lung organoid culture model for studying bat-derived infectious diseases. Sci. Rep. *15*, 4035. https://doi.org/10.1038/s41598-025-88621-0.

51. Kellner, M.J., Monteil, V.M., Zelger, P., Pei, G., Jiao, J., Onji, M., Nayak, K., Zilbauer, M., Balkema-Buschmann, A., Dorhoi, A., et al. (2025). Bat organoids reveal antiviral responses at epithelial surfaces. Nat. Immunol. *26*, 934–946. https://doi.org/10.1038/s41590-025-02155-1.

52. Uemura, K., Sasaki, M., Sanaki, T., Toba, S., Takahashi, Y., Orba, Y., Hall, W.W., Maenaka, K., Sawa, H., and Sato, A. (2021). MRC5 cells engineered to express ACE2 serve as a model system for the discovery of antivirals targeting SARS-CoV-2. Sci. Rep. *11*, 5376. https://doi.org/10.1038/s41598-021-84882-7.

53. Miao, G., Zhao, H., Li, Y., Ji, M., Chen, Y., Shi, Y., Bi, Y., Wang, P., and Zhang, H. (2021). ORF3a of the COVID-19 virus SARS-CoV-2 blocks HOPS complex-mediated assembly of the SNARE complex required for autolysosome formation. Dev. Cell *56*, 427–442.e5. https://doi.org/10.1016/j.devcel.2020.12.010.

54. Hayn, M., Hirschenberger, M., Koepke, L., Nchioua, R., Straub, J.H., Klute, S., Hunszinger, V., Zech, F., Prelli Bozzo, C., Aftab, W., et al. (2021). Systematic functional analysis of SARS-CoV-2 proteins uncovers viral innate immune antagonists and remaining vulnerabilities. Cell Rep. *35*, 109126. https://doi.org/10.1016/j.celrep.2021.109126.

55. Morales, A.E., Dong, Y., Brown, T., Baid, K., Kontopoulos, D.-G., Gonzalez, V., Huang, Z., Ahmed, A.-W., Bhuinya, A., Hilgers, L., et al. (2025). Bat genomes illuminate adaptations to viral tolerance and disease resistance. Nature *638*, 449–458. https://doi.org/10.1038/s41586-024-08471-0.

56. Agod, Z., Fekete, T., Budai, M.M., Varga, A., Szabo, A., Moon, H., Boldogh, I., Biro, T., Lanyi, A., Bacsi, A., et al. (2017). Regulation of type I interferon responses by mitochondria-derived reactive oxygen species in plasmacytoid dendritic cells. Redox Biol. *13*, 633–645. https://doi.org/10.1016/j.redox.2017.07.016.

57. Manoharan, R.R., Prasad, A., Pospíšil, P., and Kzhyshkowska, J. (2024). ROS signaling in innate immunity via oxidative protein modifications. Front. Immunol. *15*, 1359600. https://doi.org/10.3389/fimmu.2024.1359600.

58. Haller, S.L., Peng, C., McFadden, G., and Rothenburg, S. (2014). Poxviruses and the evolution of host range and virulence. Infect. Genet. Evol. *21*, 15–40. https://doi.org/10.1016/j.meegid.2013.10.014.

59. Perez-Riverol, Y., Bandla, C., Kundu, D.J., Kamatchinathan, S., Bai, J., Hewapathirana, S., John, N.S., Prakash, A., Walzer, M., Wang, S., et al. (2025). The PRIDE database at 20 years: 2025 update. Nucleic Acids Res. *53*, D543–D553. https://doi.org/10.1093/nar/gkae1011.

60. Choi, H., Larsen, B., Lin, Z.-Y., Breitkreutz, A., Mellacheruvu, D., Fermin, D., Qin, Z.S., Tyers, M., Gingras, A.-C., and Nesvizhskii, A.I. (2011). SAINT: probabilistic scoring of affinity purification-mass spectrometry data. Nat. Methods *8*, 70–73. https://doi.org/10.1038/nmeth.1541.

61. Chiem, K., Ye, C., and Martinez-Sobrido, L. (2020). Generation of recombinant SARS-CoV-2 using a bacterial artificial chromosome. Curr. Protoc. Microbiol. *59*, e126. https://doi.org/10.1002/cpmc.126.

62. Ye, C., Chiem, K., Park, J.-G., Oladunni, F., Platt, R.N., 2nd, Anderson, T., Almazan, F., de La Torre, J.C., and Martinez-Sobrido, L. (2020). Rescue of SARS-CoV-2 from a single bacterial artificial chromosome. mBio *11*, e02168-20. https://doi.org/10.1128/mBio.02168-20.

63. Gonzalez-Reiche, A.S., Alshammary, H., Schaefer, S., Patel, G., Polanco, J., Carreño, J.M., Amoako, A.A., Rooker, A., Cognigni, C., Floda, D., et al. (2023). Sequential intrahost evolution and onward transmission of SARS-CoV-2 variants. Nat. Commun. *14*, 3235. https://doi.org/10.1038/s41467-023-38867-x.

64. Khalil, Z., Sullivan, M., Gonzalez-Reiche, A.S., Obla, A., and van Bakel, H. (2023). VRAPID: Virus Reference-Based Assembly Pipeline and Identification Zenodo. https://doi.org/10.5281/zenodo.782934.

65. Aksamentov, I., Roemer, C., Hodcroft, E., and Neher, R. (2021). Nextclade: clade assignment, mutation calling and quality control for viral genomes. J. Open Source Softw. *6*, 3773. https://doi.org/10.21105/joss.03773.

66. O'Toole, Á., Scher, E., Underwood, A., Jackson, B., Hill, V., McCrone, J.T., Colquhoun, R., Ruis, C., Abu-Dahab, K., Taylor, B., et al. (2021). Assignment of epidemiological lineages in an emerging pandemic using the pangolin tool. Virus Evol. *7*, veab064. https://doi.org/10.1093/ve/veab064.

67. ARTIC Network (2020). ARTIC Network provides protocol for rapid, accurate sequencing of novel coronavirus (nCoV-2019). https://artic.network/news-ncov (accessed May 6, 2026).

68. Wilkinson, S. (2026). fieldbioinformatics: The ARTIC field bioinformatics pipeline. GitHub. https://github.com/artic-network/fieldbioinformatics.

69. Krueger, F. (2015). Trim galore. A wrapper tool around Cutadapt and FastQC to consistently apply quality and adapter trimming to FastQ files. https://www.bioinformatics.babraham.ac.uk/projects/trim_galore/.

70. Babraham, Bioinformatics. (2023). FastQC A Quality Control tool for High Throughput Sequence Data. https://www.bioinformatics.babraham.ac.uk/projects/fastqc/.

71. Ewels, P., Magnusson, M., Lundin, S., and Käller, M. (2016). MultiQC: summarize analysis results for multiple tools and samples in a single report. Bioinformatics *32*, 3047–3048. https://doi.org/10.1093/bioinformatics/btw354.

72. Grabherr, M.G., Haas, B.J., Yassour, M., Levin, J.Z., Thompson, D.A., Amit, I., Adiconis, X., Fan, L., Raychowdhury, R., Zeng, Q., et al. (2011). Full-length transcriptome assembly from RNA-Seq data without a reference genome. Nat. Biotechnol. *29*, 644–652. https://doi.org/10.1038/nbt.1883.

73. Margoliash, E. (1963). Primary structure and evolution of cytochrome c. Proc. Natl. Acad. Sci. USA *50*, 672–679. https://doi.org/10.1073/pnas.50.4.672.

74. Li, H. (2026). seqtk: Toolkit for processing sequences in FASTA/Q formats (GitHub). https://github.com/lh3/seqtk.

75. Chiva, C., Olivella, R., Borràs, E., Espadas, G., Pastor, O., Solé, A., and Sabidó, E. (2018). QCloud: A cloud-based quality control system for mass spectrometry-based proteomics laboratories. PLoS One *13*, e0189209. https://doi.org/10.1371/journal.pone.0189209.

76. Cox, J., and Mann, M. (2008). MaxQuant enables high peptide identification rates, individualized p.p.b.-range mass accuracies and proteome-wide protein quantification. Nat. Biotechnol. *26*, 1367–1372. https://doi.org/10.1038/nbt.1511.

77. Sonnhammer, E.L.L., and Östlund, G. (2015). InParanoid 8: orthology analysis between 273 proteomes, mostly eukaryotic. Nucleic Acids Res. *43*, D234–D239. https://doi.org/10.1093/nar/gku1203.

78. Sievers, F., and Higgins, D.G. (2021). The Clustal Omega multiple alignment package. Methods Mol. Biol. *2231*, 3–16. https://doi.org/10.1007/978-1-0716-1036-7_1.

79. Shannon, P., Markiel, A., Ozier, O., Baliga, N.S., Wang, J.T., Ramage, D., Amin, N., Schwikowski, B., and Ideker, T. (2003). Cytoscape: a software environment for integrated models of biomolecular interaction networks. Genome Res. *13*, 2498–2504. https://doi.org/10.1101/gr.1239303.

80. Tsitsiridis, G., Steinkamp, R., Giurgiu, M., Brauner, B., Fobo, G., Frishman, G., Montrone, C., and Ruepp, A. (2023). CORUM: the comprehensive resource of mammalian protein complexes-2022. Nucleic Acids Res. *51*, D539–D545. https://doi.org/10.1093/nar/gkac1015.

81. Rhie, A., McCarthy, S.A., Fedrigo, O., Damas, J., Formenti, G., Koren, S., Uliano-Silva, M., Chow, W., Fungtammasan, A., Kim, J., et al. (2021). Towards complete and error-free genome assemblies of all vertebrate species. Nature *592*, 737–746. https://doi.org/10.1038/s41586-021-03451-0.

82. Li, H. (2023). Protein-to-genome alignment with miniprot. Bioinformatics *39*, btad014. https://doi.org/10.1093/bioinformatics/btad014.

83. Ranwez, V., Chantret, N., and Delsuc, F. (2021). Aligning protein-coding nucleotide sequences with MACSE. Methods Mol. Biol. *2231*, 51–70. https://doi.org/10.1007/978-1-0716-1036-7_4.

84. Capella-Gutiérrez, S., Silla-Martínez, J.M., and Gabaldón, T. (2009). trimAl: a tool for automated alignment trimming in large-scale phylogenetic analyses. Bioinformatics *25*, 1972–1973. https://doi.org/10.1093/bioinformatics/btp348.

85. Altschul, S.F., Madden, T.L., Schäffer, A.A., Zhang, J., Zhang, Z., Miller, W., and Lipman, D.J. (1997). Gapped BLAST and PSI-BLAST: a new generation of protein database search programs. Nucleic Acids Res. *25*, 3389–3402. https://doi.org/10.1093/nar/25.17.3389.

86. Huber, W., Carey, V.J., Gentleman, R., Anders, S., Carlson, M., Carvalho, B.S., Bravo, H.C., Davis, S., Gatto, L., Girke, T., et al. (2015). Orchestrating high-throughput genomic analysis with Bioconductor. Nat. Methods *12*, 115–121. https://doi.org/10.1038/nmeth.3252.

87. Hughes, C.S., Moggridge, S., Müller, T., Sorensen, P.H., Morin, G.B., and Krijgsveld, J. (2019). Single-pot, solid-phase-enhanced sample preparation for proteomics experiments. Nat. Protoc. *14*, 68–85. https://doi.org/10.1038/s41596-018-0082-x.

88. Li, J., Cai, Z., Vaites, L.P., Shen, N., Mitchell, D.C., Huttlin, E.L., Paulo, J.A., Harry, B.L., and Gygi, S.P. (2021). Proteome-wide mapping of short-lived proteins in human cells. Mol. Cell *81*, 4722–4735.e5. https://doi.org/10.1016/j.molcel.2021.09.015.

89. Wu, G., and Haw, R. (2017). Functional interaction network construction and analysis for disease discovery. Methods Mol. Biol. *1558*, 235–253. https://doi.org/10.1007/978-1-4939-6783-4_11.

90. Ewels, P.A., Peltzer, A., Fillinger, S., Patel, H., Alneberg, J., Wilm, A., Garcia, M.U., Di Tommaso, P., and Nahnsen, S. (2020). The nf-core framework for community-curated bioinformatics pipelines. Nat. Biotechnol. *38*, 276–278. https://doi.org/10.1038/s41587-020-0439-x.

91. Chen, S. (2023). Ultrafast one-pass FASTQ data preprocessing, quality control, and deduplication using fastp. Imeta *2*, e107. https://doi.org/10.1002/imt2.107.

92. Dobin, A., Davis, C.A., Schlesinger, F., Drenkow, J., Zaleski, C., Jha, S., Batut, P., Chaisson, M., and Gingeras, T.R. (2013). STAR: ultrafast universal RNA-seq aligner. Bioinformatics *29*, 15–21. https://doi.org/10.1093/bioinformatics/bts635.

93. Patro, R., Duggal, G., Love, M.I., Irizarry, R.A., and Kingsford, C. (2017). Salmon provides fast and bias-aware quantification of transcript expression. Nat. Methods *14*, 417–419. https://doi.org/10.1038/nmeth.4197.

94. Soneson, C., Love, M.I., and Robinson, M.D. (2015). Differential analyses for RNA-seq: transcript-level estimates improve gene-level inferences. F1000Res *4*, 1521. https://doi.org/10.12688/f1000research.7563.2.

95. Love, M.I., Huber, W., and Anders, S. (2014). Moderated estimation of fold change and dispersion for RNA-seq data with DESeq2. Genome Biol. *15*, 550. https://doi.org/10.1186/s13059-014-0550-8.

96. Yu, G., Wang, L.-G., Han, Y., and He, Q.-Y. (2012). clusterProfiler: an R package for comparing biological themes among gene clusters. OMICS *16*, 284–287. https://doi.org/10.1089/omi.2011.0118.

97. Gu, Z., Eils, R., and Schlesner, M. (2016). Complex heatmaps reveal patterns and correlations in multidimensional genomic data. Bioinformatics *32*, 2847–2849. https://doi.org/10.1093/bioinformatics/btw313.

98. Barrett, T., Wilhite, S.E., Ledoux, P., Evangelista, C., Kim, I.F., Tomashevsky, M., Marshall, K.A., Phillippy, K.H., Sherman, P.M., Holko, M., et al. (2013). NCBI GEO: archive for functional genomics data sets–update. Nucleic Acids Res. *41*, D991–D995. https://doi.org/10.1093/nar/gks1193.

99. Webb, B., and Sali, A. (2016). Comparative protein structure modeling using MODELLER. Curr. Protoc. Bioinform. *54*, 5.6.1–5.6.37. https://doi.org/10.1002/cpbi.3.

100. Schymkowitz, J., Borg, J., Stricher, F., Nys, R., Rousseau, F., and Serrano, L. (2005). The FoldX web server: an online force field. Nucleic Acids Res. *33*, W382–W388. https://doi.org/10.1093/nar/gki387.

101. Sallard, E., Halloy, J., Casane, D., Decroly, E., and van Helden, J. (2021). Tracing the origins of SARS-COV-2 in coronavirus phylogenies: a review. Environ. Chem. Lett. *19*, 769–785. https://doi.org/10.1007/s10311-020-01151-1.

102. Asero, R., Abbadessa, S., Aruanno, A., Barilaro, G., Barzaghi, C., Bignardi, D., Bilò, M.B., Borro, M., Bresciani, M., Busa, M., et al. (2021). Sensitization to gibberellin-regulated protein (peamaclein) among Italian cypress pollen-sensitized patients. J. Investig. Allergol. Clin. Immunol. *32*, 40–47. https://doi.org/10.18176/jiaci.0542.

103. Katoh, K., and Standley, D.M. (2013). MAFFT multiple sequence alignment software version 7: improvements in performance and usability. Mol. Biol. Evol. *30*, 772–780. https://doi.org/10.1093/molbev/mst010.

104. Ranwez, V., Douzery, E.J.P., Cambon, C., Chantret, N., and Delsuc, F. (2018). MACSE *v2*: Toolkit for the alignment of Coding Sequences accounting for frameshifts and stop codons. Mol. Biol. Evol. *35*, 2582–2584. https://doi.org/10.1093/molbev/msy159.

105. Guindon, S., Dufayard, J.-F., Lefort, V., Anisimova, M., Hordijk, W., and Gascuel, O. (2010). New algorithms and methods to estimate maximum-likelihood phylogenies: assessing the performance of PhyML 3.0. Syst. Biol. *59*, 307–321. https://doi.org/10.1093/sysbio/syq010.

106. Thinnes, C.C., Lohans, C.T., Abboud, M.I., Yeh, T.-L., Tumber, A., Nowak, R.P., Attwood, M., Cockman, M.E., Oppermann, U., Loenarz, C., et al. (2019). Selective inhibitors of a human prolyl hydroxylase (OGFOD1) involved in ribosomal decoding. Chemistry *25*, 2019–2024. https://doi.org/10.1002/chem.201804790.

107. Zhou, L., Feng, T., Xu, S., Gao, F., Lam, T.T., Wang, Q., Wu, T., Huang, H., Zhan, L., Li, L., et al. (2022). Ggmsa: A visual exploration tool for multiple sequence alignment and associated data. Brief. Bioinform. *23*, bbac222. https://doi.org/10.1093/bib/bbac222.

108. Chen, C., Nadeau, S., Yared, M., Voinov, P., Xie, N., Roemer, C., and Stadler, T. (2022). CoV-Spectrum: analysis of globally shared SARS-CoV-2 data to identify and characterize new variants. Bioinformatics *38*, 1735–1737. https://doi.org/10.1093/bioinformatics/btab856.

109. Elbe, S., and Buckland-Merrett, G. (2017). Data, disease and diplomacy: GISAID's innovative contribution to global health. Glob. Chall. *1*, 33–46. https://doi.org/10.1002/gch2.1018.

Please cite this article in press as: Batra et al., Coronavirus protein interaction mapping in bat and human cells reveals network rewiring governing immune evasion and zoonotic potential, Cell Host & Microbe (2026), https://doi.org/10.1016/j.chom.2026.04.015

STAR★METHODS

KEY RESOURCES TABLE

REAGENT or RESOURCE	SOURCE	IDENTIFIER
Antibodies		
Strep-Tag Antibody	Qiagen	Cat# 34850; RRID: AB_2810987
Flag-Tag Antibody	Sigma-Aldrich	Cat# F3165; RRID: AB_259529
β-Actin Antibody	Cell Signaling Technology	Cat# 4970; RRID: AB_2223172
TOM70 Antibody	Santa Cruz Biotechnology	Cat# sc-390545; RRID: AB_2714192
MTARC2 Antibody	Invitrogen	Cat# PA5-53276; RRID: AB_2644060
alpha-Tubulin Antibody	Cell Signaling Technology	Cat# 2144; RRID: AB_2210548
β-Tubulin Antibody	Sigma-Aldrich	Cat# T8328; RRID: AB_1844090
Anti-rabbit IgG, HRP-linked Antibody	Cell Signaling Technology	Cat# 7074; RRID: AB_2099233
Anti-mouse IgG, HRP-linked Antibody	Cell Signaling Technology	Cat# 7076; RRID: AB_330924
Anti-SARS-CoV-2 Nucleocapsid antibody	Center for Therapeutic Antibody Development (CTAD), Icahn School of Medicine at Mount Sinai	Cat# 1C7C7; RRID: AB_2893978
Anti-SARS-CoV-2 (COVID-19) ORF9b antibody [HL1918]	Genetex	Cat# GTX637667; RRID: AB_3741055
Human/Mouse/Rat/Hamster ACE-2 Antibody	R&D Systems	Cat# AF933; RRID: AB_355722
TMPRSS2 Polyclonal Antibody	Invitrogen	Cat# PA5-143839; RRID: AB_3075053
Rabbit IgG Isotype Control	Fisher Scientific	Cat# 26102; RRID: AB_2532938
Bacterial and Virus Strain		
Stellar™ Competent Cells	Takara	Cat# 636766
SARS-CoV-2, isolate USA-WA1/2020	BEI Resources	Cat# NR-52281
rSARS-CoV-2 N_P80T	This paper	N/A
rSARS-CoV-2 N_P80T, ORF9b_T72I	This paper	N/A
rSARS-CoV-2 NSP4_T269I	This paper	N/A
Chemicals, Peptides, and Recombinant Proteins		
Lipofectamine 2000	Invitrogen	Cat# 11668500
PolyJet	SignaGen Laboratories	Cat# SL100688
Protease inhibitor cocktail	Sigma Aldrich (Roche)	Cat# 11836170001
PhosSTOP Phosphatase Inhibitor	Sigma-Aldrich	Cat# 4906845001
Doxycycline	Clontech	Cat# 631311
Blasticidin	Invivogen	Cat# ant-bl-05
Puromycin	Invivogen	Cat# ant-pr-1
Hygromycin B	Life Technologies	Cat# 10687010
Nonidet P 40 Substitute	Fluka Analytical/Sigma-Aldrich	Cat# 74385
Sequencing Grade Modified Trypsin	Promega	Cat# V5113
Alt-R S.p. Cas9 Nuclease V3	IDT	Cat# 1081059
Alt-R HDR Enhancer V2	IDT	Cat# 10007910
Commercial Assays kits		
QIAGEN Plasmid Plus Maxi Kit	QIAGEN	Cat# 12963
RNeasy Mini Kit	QIAGEN	Cat# 74104
GeneJet Gel Extraction Kit	Life Technologies	Cat# K0691
QIAquick PCR Purification Kit	QIAGEN	Cat# 28104

(*Continued on next page*)

Continued

REAGENT or RESOURCE	SOURCE	IDENTIFIER
QUANTI-Luc™ 4 Lucia/Gaussia	Invivogen	Cat# rep-qlc4lg1
SuperScript™ IV First-Strand Synthesis System	ThermoFisher Scientific	Cat# 18091200
P3 Primary Cell 4D-Nucleofector™ X Kit S	Lonza	Cat# V4XP-3032
Universal Mycoplasma Detection Kit	ATCC	Cat# 30-1012K
Native Barcoding Kit 24 V14	Oxford Nanopore Technologies	Cat# SQK-NBD114.24
MinION flow cell (R.9.4.1)	Oxford nanopore	Cat# FLO-MIN106D
RiboPure kit	Invitrogen	Cat# AM1924
ONE-Glo Luciferase Assay System kit	Promega	Cat# E6110
miRNeasy mini kit	QIAGEN	Cat# 217004
P3 nucleofector kit	Lonza	Cat# V4XP-3032
SE Cell Line 4D-Nucleofector® X Kit S	Lonza	Cat# V4XC-1032
Pierce™ Direct Magnetic IP/Co-IP Kit	Thermo Scientific	Cat# PI88828
Deposited data		
AP-MS	This paper	PRIDE[59] project ID: PXD065873
RNAseq data from bat and human cells infected with SARS-CoV-2	This paper	GEO: GSE302357
Experimental Models: Mammalian Cells		
HEK293T	UCSF's Cell and Genome Engineering Core	(https://cgec.ucsf.edu/cell-culture-and-banking-services, cell line collection: CCLZR076)
HEK293T	ATCC	Cat# CRL-3216
HEK293T-AT	BEI Resources	NR-55293
RFe	This paper	N/A
RFe-AT	This paper	N/A
MRC5	ATCC	Cat# 50188319FP
MRC5-ACE2	This paper	N/A
Lenti-X HEK293T	Takara Bio	Cat# 632180
Vero E6	ATCC	Cat# CRL-1586
TMPRSS2-Vero E6	(BPS Bioscience	Cat# 78081
Recombinant DNA		
pLVX-TetOne-Puro SARS-CoV-2 plasmids	This paper	N/A
pLVX-EF1a-Puro SARS-CoV-2 plasmids	Gordon et al.[12]	N/A
pLVX-TetOne-Puro RaTG13 plasmids	This paper	N/A
pLVX-EF1a-Puro RaTG13 plasmids	This paper	N/A
pWPI-IRES-Bla-Ak-ACE2	Addgene	Plasmid# 154981
pTRIP-SFFV-Hygro-2A-TMPRSS2	Addgene	Plasmid# 170390
SV40 1: pBSSVD2005	Addgene	Plasmid# 21826
Human Tom70-flag pcDNA	Genscript	Clone ID: OHu09660 (NM_014820.5)
Human MTARC2-flag pcDNA	Genscript	CloneID: OHu17176 (NM_017898.5)
psPAX2	Addgene	Plasmid# 12260
pMD2.G	Addgene	Plasmid# 12259
pcDNA3.1_hACE2	Addgene	Plasmid# 145033
pcDNA3.1_RfACE2	Genscript	Clone ID: GCF_004115265.2 (XM_033107295)
Plasmid SV40 1: pBSSVD2005	Addgene	Plasmid# 21826
pNL4-3.Luc.R-E- vector	NovoPro	Cat. No.: V012797
SARS-CoV-2Δ19 plasmid	Invitrogen	https://www.invivogen.com/sars2-spike-vectors
Oligonucleotides		
RFe RPL13A Forward CGCCAAGGCTTCCTTCTTTC	This paper	N/A

(*Continued on next page*)

Please cite this article in press as: Batra et al., Coronavirus protein interaction mapping in bat and human cells reveals network rewiring governing immune evasion and zoonotic potential, Cell Host & Microbe (2026), https://doi.org/10.1016/j.chom.2026.04.015

Continued

REAGENT or RESOURCE	SOURCE	IDENTIFIER
RFe RPL13A Reverse GGTTGGTGTTCATCCGCTTG	This paper	N/A
RFe Mx1 Forward TTCCTCTGATTGTCCAGTTC	This paper	N/A
RFe Mx1 Reverse CCTCTTGTCGCTGGTGTCA	This paper	N/A
RFe ISG15 Forward GCCCACAGCCATGATAGGG	This paper	N/A
RFe ISG15 Reverse CTGCTTCAGGTCCGCTGTAA	This paper	N/A
Human TBP Forward GCACTGATTTTCAGTTCTGG	This paper	N/A
Human TBP Reverse GCTGGAAAACCCAACTTCTGT	This paper	N/A
Human Mx1 Forward GTGGCTGAGAACAACCTGRG	This paper	N/A
Human Mx1 Reverse GGCATCTGGTCACGATCCC	This paper	N/A
Human ISG15 Forward TCCTGGTGAGGAA TAACAAGGG	This paper	N/A
Human ISG15 Reverse GTCAGCCAGAACAGGTCGTC	This paper	N/A
Human ACE2 Forward GGACCCAGGAAATGTTCAGA	This paper	N/A
Human ACE2 Reverse GGCTGCAGAAAGTGACATGA	This paper	N/A
Human TMPRSS2 Forward CAAGTGCTC CAACTCTGGGGAT	This paper	N/A
Human TMPRSS2 Reverse AACACACCG ATTCTCGTCCTC	This paper	N/A
Bat ACE2 Forward TGACTGGGTTTTGAACAGTGCC	This paper	N/A
Bat ACE2 Reverse TGGATTGAGCAGCGGTTACA	This paper	N/A
Bat TMPRSS2 Forward CAAGTGCTCGGTGTCCGGGAT	This paper	N/A
Bat TMPRSS2 Reverse AACGCACCGGTTCTCGTCCTC	This paper	N/A
Bat Tom70 Forward CAAGTCGGAAA TGGAGATGGCTCATTTATACTCACTCTG	This paper	N/A
Bat Tom70 Reverse CACAACACCTAACT GAGAAACAGGTGTGACAATGAC	This paper	N/A
Bat Tom70_seq GCTCATTTATACTCACTCTGTGATG	This paper	N/A
Strep Reverse CTGAGGGTGAGACCATGC ACTTCCACCTGATC	This paper	N/A
gRNA sequences		
Bat_Tom70 CCCATATTTTATAATGTTGG	This paper	N/A
Software and Algorithms		
GraphPad Prism 7	GraphPad Software	https://www.graphpad.com
MiST	Verschueren et al.[15]	N/A
SAINT	Choi et al.[60]	N/A
MinKNOW	Oxford Nanopore	https://nanoporetech.com/products/minion
Other		
MagStrep “type3” XT beads	IBA Lifesciences	Cat# 2-4090-002
BioPureSPE Mini 96-Well, 20mg PROTO 300 C18, 7-70µg	Nest group	Cat# HNS S18V
4–20% Criterion™ TGX™ Gel, 18 well	Bio-Rad Laboratories	Cat# 567-1094
4–20% Criterion™ TGX™ Gel, 26 well	Bio-Rad Laboratories	Cat# 567-1095

EXPERIMENTAL MODEL AND SUBJECT DETAILS

Capturing and sampling of greater horseshoe bats

We sampled a colony of a few hundred individuals of the greater horseshoe bat species (*R. ferrumequinum*) occupying the tunnels of an abandoned water network system opening in a forest of evergreen oaks (Quercus ilex) with pastures near Jerez de la Frontera, Cádiz, Southern Spain in May 2020. In order to minimize disturbances to the colony, only an adult male bat and a pregnant female bat resting isolated from the group were captured with the help of a hand net. Following the guidelines of the American Society of Mammalogists (2016) and with the approval of the Spanish bio-ethical authority and the Andalusian regional government, the two

bats were euthanized by cervical dislocation. Immediately after, bats were dissected and skin and lung samples together with the large bones (arms and legs) were preserved in a volume of 15 ml of RPMI medium in individual falcon tubes. Similarly, the fetus was beheaded and minced and preserved in RPMI medium. All samples were stored at 4 °C and processed in the lab within 25-30 hours of collection.

Establishment of bat primary lung fibroblasts

Tissue samples from lungs were obtained as described above to establish bat primary cell cultures. Briefly, tissue fragments were incubated for 30 to 60 min at 37°C in a solution of 0.2 Wünsch units/ml of Liberase (Sigma-Aldrich) in Dulbecco's Modified Eagle Medium/Nutrient Mixture F-12 (DMEM/F-12) (Thermo Fisher) and 1% penicillin-streptomycin (10,000 U/mL) (Thermo Fisher). Digestion was stopped by adding DMEM/F-12 supplemented with 15% fetal bovine serum (FBS) (Peak Serum) and 1% penicillin-streptomycin (10,000 U/mL). The tissue was mechanically dislodged by pipetting, followed by multiple centrifugations and washing steps. The pellet was resuspended and plated in a cell culture flask and incubated at 37°C in 5% CO_2 for 5 to 7 days to allow cell migration from within the tissue fragments and attachment to the flask surface. Cells were then cultured in DMEM/F-12 medium supplemented with 10% FBS (Peak Serum) and 1% penicillin-streptomycin (10,000 U/mL) (Thermo Fisher).

Immortalization of bat primary lung fibroblasts

Primary lung fibroblasts were immortalized by nucleofection with a SV40-LT antigen expressing construct (Addgene plasmid #21826, a gift from David Ron). Nucleofection was performed using P3 Primary Cell 4D-Nucleofector™ X Kit S following the protocol recommended for the transfection of primary cell lines. Briefly, 1×10^5 cells were resuspended in a nucleofection mixture containing 16.4 μL P3 Nucleofector Solution, 3.6 μL Supplement reagent, and 0.5 μg SV40-LT plasmid DNA. Cells were electroporated using an Amaxa 4D-Nucleofector™ X Unit. Following nucleofection, cells were transferred into fresh culture medium. Cells were then cultured in DMEM/F-12 medium supplemented with 10% FBS (Peak Serum) and 1% penicillin-streptomycin (10,000 U/mL) (Thermo Fisher) at 37°C with 5% CO_2. Medium was replaced 24 h post-nucleofection to remove cellular debris and non-adherent cells and subsequently refreshed every 2–3 days. Cells were monitored for recovery and proliferative outgrowth over the following 7–14 days. Once proliferating cell populations were evident, cultures were expanded gradually and passaged upon reaching ~70–80% confluence. Cells exhibiting sustained proliferation over multiple passages without signs of senescence were considered stably immortalized and used for downstream experiments.

Generation of greater horseshoe bat lung fibroblasts stably expressing human ACE2 and TMPRSS2

Greater horseshoe bat lung fibroblasts stably expressing human ACE2 and TMPRSS2 cells (RFe-AT) were generated through lentiviral transduction. To generate lentiviruses, HEK293T cells were transfected with human ACE2 or TMPRSS2 lentiviral plasmids (Addgene #154981 and #170390, respectively), along with packaging plasmids for Gag-Pol (psPAX2) and VSV-G (pMD2.G) in a 15 cm dish. At 72 hours post-transfection, the supernatant was collected and filtered using a 0.45μm PVDF filter unit. Filtered virus supernatant was mixed with 8.5% PEG-6000 and 0.3M NaCl and incubated for at least 2 hours for precipitation. The virions were pelleted by centrifugation in a spinning bucket rotor at 3500 x g for 45 minutes at 4°C and resuspended in phosphate-buffered saline (PBS). For transduction, cells were trypsinized and spinoculated with hACE2 lentiviruses and 8μg/ml polybrene at 800 x g for 1 hour at room temperature. Cell pellet was then resuspended in fresh media and cultured for 96 hours. Cells were selected with 5μg/ml blasticidin for 3-4 days until non-transduced cells were dead. These cells were further spinoculated with hTMPRSS2 lentiviruses and transduced cells were selected with 250μg/ml hygromycin (Thermo Fisher). Expression of hACE2 and TMPRSS2 was validated by western blot with anti-ACE2 (Cell Signaling) and anti-TMPRSS2 antibody (Invitrogen).

Generation of greater horseshoe bat lung fibroblasts stably expressing bat Tom70 or MTARC2

Bat Tom70 and MTARC2 were cloned into the pLVX-EF1α-IRES-Puro vector (Takara/Clontech) without any tag. Lentiviruses were generated as described above and used to transduce RFe-AT cells. Transduced cells were selected with 2.5 μg/mL puromycin until all non-transduced control cells were dead. Expression of bTom70 and bMTARC2 was validated by western blot using anti-Tom70 (Santa Cruz Biotechnology) and anti-MTARC2 (Invitrogen) antibodies.

Cell culture

Human embryonic kidney cells with epithelial morphology (HEK293T/17) cells were maintained in Dulbecco's Modified Eagle Medium (DMEM; Corning), supplemented with 10% fetal bovine serum (FBS; Gibco, Life Technologies) and 1% penicillin–streptomycin (Corning). Cells were cultured at 37 °C in a humidified incubator with 5% CO_2. The HEK293T/17 cell line was obtained from the UCSF Cell Culture Facility and cell line authentication was performed by the Berkeley Cell Culture Facility via STR profiling in August, 2017, confirming a 94% match with the reference HEK293T/17 profile. RFe cells were cultured in DMEM/F-12 medium supplemented with 10% FBS (Gibco, Life Technologies) and 1% penicillin-streptomycin (10,000 U/mL) (Thermo Fisher). Vero E6 (ATCC, CRL-1586) and TMPRSS2-Vero E6 (BPS Bioscience Cat# 78081) were maintained in Dulbecco's modified Eagle's medium (DMEM) (Corning) supplemented with 10% FBS (Peak Serum), 1% MEM non-essential amino acids solution (100x) (Gibco), 1% HEPES (N-2-hydroxyethylpiperazine-N-2-ethane sulfonic acid) (1M) (Gibco) and 1% penicillin/streptomycin (10,000 U/mL) (Corning) at 37 °C and 5% CO_2. HEK293T (ATCC, CRL-3216), HEK293T AT (BEI Resources, NR-55293), and MRC5 (ATTC, CCL-171) were maintained in DMEM (Corning) supplemented with 10% fetal bovine serum (Peak Serum) and 1% penicillin/streptomycin (10,000 U/mL) (Corning)

at 37°C and 5% CO_2. MRC5 hACE2 were generated for this study by transduction with lentiviruses applying the same protocol as for RFe-AT cells described above. All cell lines used in this study were regularly screened for Mycoplasma contamination, using the Universal Mycoplasma Detection Kit (ATCC, 30-1012K).

Viruses and infections

Virus infections were performed using SARS-CoV-2, isolate USA-WA1/2020 (BEI Resources NR-52281). Additionally, four recombinant SARS-CoV-2 viruses, based on the USA-WA1/2020 reference sequence were used. The rSARS-CoV-2 WT have been previously described.[61] A recombinant virus with a single amino acid substitution in Nucleocapsid at position 80 (rSARS-CoV-2 N_P80T), a recombinant virus with two mutations leading to amino acid substitutions in Nucleocapsid at position 80 and in ORF9b at position 72 (rSARS-CoV-2 N_P80T, ORF9b_T72I), recombinant virus with a single amino acid substitution in Nonstructural Protein 4 (NSP4_T269I), were generated for this study, using the same bacterial artificial chromosome (BAC)-based SARS-CoV-2 reverse genetic system previously described.[62] Briefly, one or two oligonucleotides were used to introduce N_P80T, ORF9b_T72I or NSP4T_269I coding changes into fragment 1 by site-directed mutagenesis. The region in the wild-type BAC between the unique restriction sites of BamHI and RsrII was replaced by the one from fragment 1 containing the mutation, and the newly generated BAC was used to produce the recombinant mutant viruses according to the protocol described previously. All viral stocks were grown in Vero E6 TMPRSS2 cells and validated by genome sequencing. Virus growth media (VGM) was used for all infections: Dulbecco's modified Eagle's medium (Corning) supplemented with 2% fetal bovine serum (Peak Serum), 1% non-essential amino acids (Gibco), 1% HEPES (Gibco) and 1% penicillin/streptomycin (Corning) at 37 °C and 5% CO_2. Influenza A viruses A/Puerto Rico/8/1934 (H1N1) and A/WSN/1933 (H1N1) were grown in the allantoic cavity of 8-10 day-old embryonated eggs for 48h at 37 °C. Allantoic fluid was then harvested, clarified by centrifugation (3000 rpm, 5 min, 4°C) and stored at -80°C. Viral titers were determined by standard plaque assay on MDCK cells. The Vesicular stomatitis Indiana virus VSV-GFP-M51 stock was grown in BHK21 cells in VGM media (DMEM, 2% FBS, 1% P/S, 1% HEPES, 1% NEAA). Stock was titrated in BHK21 cells. Gibco Opti-MEM Reduced Serum Media was used for influenza and VSV-GFP-M51 infections.

METHOD DETAILS

Virus stock sequencing

Following viral RNA extraction using the Ribo Pure RNA Purification kit (Thermo Fisher Scientific) according to the manufacturer's instructions, stocks were sequenced on the Oxford Nanopore MinION or Illumina MiSeq platforms. Samples sequenced on the Illumina MiSeq platform underwent cDNA synthesis using ProtoScript II (New England Biolabs, cat. E6560), followed by whole-genome amplification with two custom, interleaved tiling primer panels, as previously described.[63] PCR amplification was carried out using Q5 Hot Start High-Fidelity DNA polymerase (New England Biolabs, cat. M0493) in 25 μL reaction volumes. The resulting amplicons were purified using a 1.8X ratio of Ampure XT beads (Beckman Coulter, A63882) and used as input for library preparation using the Nextera XT kit (Illumina, cat. FC-131-1096) and sequenced in paired-end mode (2×150 nt) on the Illumina MiSeq. Genome assembly and quality control were performed using our custom vRAPID pipeline.[64] Complete genomes were classified by clade and lineage using Nextclade CLI (v3.15.3)[65] and pangolin (v4.3)[66] tools. For samples sequenced on an Oxford Nanopore flowcell, the Artic Consortium protocol,[67] was used with modifications. Native barcoding of amplicons was performed with Native Barcoding Kit 24 V14 (SQK-NBD114.24), according to the manufacturer's instructions. Basecalling and demultiplexing was done with Dorado v0.9.6 (FAST5 input files) and v1.0.2 (POD5 input files) in high accuracy basecalling mode (dna_r10.4.1_e8.2_400bps_hac@v5.0.0). The genome assembly was done with the Artic pipeline (artic-network/artic-ncov2019, v.1.7.1)[68] where reads were normalized to 10,000 then aligned to the reference genome Wuhan-Hu-1 (MN908947.3) using minimap2 (2.30-r1287), consensus variants were called with clair3 (v1.1.1). The consensus sequences were then analyzed for clade and lineage classification using the Nextclade CLI (v3.15.3)[64] and pangolin (v4.3).[66]

SARS-CoV-2 adaptation to RFe-AT lung fibroblasts

RFe-AT cells were seeded at the density of 2×10^5 cells/well on 12-well plate format. The next day cells were infected with SARS-CoV-2, isolate USA-WA1/2020 at an MOI of 1. At four days post-infection, 10μl of supernatant was passaged to a new culture of RFe-AT cells. A total of three blind passages were performed. Plaque purification was performed to isolate virus from passage 3, and single plaques were used to grow stocks. Viral RNA was extracted from the supernatant of each passage and plaque purified stocks using RiboPure kit (Invitrogen, AM1924) and subjected to whole virus genome nanopore sequencing.

Generation of HIV-based pseudotyped particles

To generate HIV-based SARS-CoV-2 spike or VSV.G pseudotype particles, 5×10^6 293T cells were plated per 10-cm dish in 10 ml in growth medium. The next day, 7.5 μg pHIV-1NL4-3 ΔEnv luciferase reporter virus plasmid (pNL4-3.Luc.R-E- vector, NovoPro) and 2.5 μg SARS-CoV-2Δ19 plasmid (Invivogen) or pMD2.G (Takara) using LT-1 transfection reagent (Mirus) in DNA: reagent ratio 1:3 in 500μl of OptiMEM (Thermo Fisher) and added to cells drop-wise 20 min post incubation. At 12 hours post transfection cells were washed with PBS and 10ml of fresh medium was added. Supernatant was collected 48 hours post transfection, filtered through 0.45μm filters and aliquoted. To determine the titer of produced VLPs HEK293T cells were infected with serial 5-fold dilutions of each VLPs stock. At 48 hours post-infection cells were fixed and stained with VSV-G or SARS-CoV-2 Spike antibody, followed by

staining with secondary Alexa488 antibody. The GFP-positive cells were quantified by fluorescence microscopy. Transduction units per milliliter (TU/ml) were calculated by applying the formula: (Number of cells at transduction) × [Fraction of cells showing fluorescence / (mL of Viral Stock used)]

Pseudotyped virus entry assay

To perform virus entry study RFe, RFe-AT, HEK293T and HEK293T-AT cells were seeded on 96-well plates at a density of 1x 10 ^4 cells/well. The next day cells were infected with HIV-based SARS-CoV-2 Spike or VSV.G particles at MOI 1. At 48h post infection cells were lysed and firefly luciferase activity was assessed with ONE-Glo Luciferase Assay System kit (Promega). The readout was performed with a luminometer at a wavelength of 680nm.

Infection of HEK293T cells overexpressing ACE2 orthologs with SARS-CoV-2 WA/01 virus

The day before transfection HEK293T cells were seeded in a 12-well plate format. The next day cells were transfected with 1μg of pcDNA3.1, pcDNA3.1 plasmid carrying human ACE2 or bat ACE2 with LT-1 reagent (Mirus). The pcDNA3.1 humanACE2 was a gift from Fang Li (Addgene plasmid # 145033; http://n2t.net/addgene:145033; RRID: Addgene_145033), a pcDNA3.1 plasmid carrying greater horseshoe bat ACE2 (RfACE2) was designed and synthesized by Genewiz, based on the gene sequence available from the reference genome (NCBI RefSeq sequence: GCF_004115265.2; XM_033107295) with HA tag on its C-terminus. At 24h post transfection cells were infected with SARS-CoV-2 WA1/01 isolate at MOI 1. The next day cells were detached with PBS supplemented with 1mM EDTA (Gibco) and immunolabeled with hACE2 antibody (R&D systems, #AF933) conjugated with AlexaFluor647 (Thermo Fisher) and Fixable Viability Dye eFluor 450 (Thermo Fisher) for one hour on ice. Next cells were fixed in 4% paraformaldehyde for 15 minutes on ice, permeabilized with 1xPermWash buffer (BD Bioscience) and immunolabeled with anti-SARS-CoV-2 nucleocapsid (N) antibody conjugated to AlexaFluor488 (Thermo Fisher) for one hour on ice. Cells were washed with Cells Staining buffer (BioLegend) and resuspended in PBS prior cytometry analysis with Gallios cytometer (Beckman). At least 10,000 live cells were used to determine ACE2 expression level and infection rates for SARS-CoV-2 WA1 virus. Virus infection level in cells was measured by gating for SARS-CoV-2 nucleocapsid positive cell population.

Immunofluorescence labeling of cells with α-tubulin antibody

Cells were seeded at a density of 3×10^3 cells/well on 96 well plate format. The next day cells were fixed in 4% paraformaldehyde for 15 minutes, permeabilized with 0.1% Triton X-100 (Sigma-Aldrich) in PBS and blocked in 3% bovine serum albumin in PBS for 45 minutes. Next cells were incubated with mouse α-tubulin antibody (Cell Signaling) at a 1:200 dilution, followed by incubation with anti-mouse Alexa Fluor Plus 488 secondary antibody (Thermo Fisher Scientific) and DAPI (4',6-diamidino-2-phenylindole) in 1:1000 dilution. All antibodies were diluted in 1% bovine serum albumin in PBS. Imaging was performed with an EVOS M5000 microscope.

Species origin characterization of RFe with RNAseq

RNA was extracted from four replicates using Qiagen RNeasy kits. Library preparation and sequencing were performed by Azenta Life Science using the following conditions: rRNA depletion for mRNA and long noncoding species, standard RNAseq run in Illumina HiSeq 4000 with a depth of 20-30 million reads per sample. The integrity of the RNA sequencing files of four samples (four replicates) was checked with the md5sum utility of GNU coreutils 8.22. For cleaning the reads and trimming, the software trim_galore v0.6.7[69] was used, and to check the result of this process, FastQC v0.11.9[70] and MultiQC v1.11[71] were used. It was determined that the average quality throughout the sequence of cleaned reads was greater than a Phred Score of 35, so the analysis began. In order to obtain a robust result in verifying the species from which the samples came, it was decided to assemble the transcriptome of the four samples separately. For this purpose, the software Trinity v2.12.0[72] was used. Once the transcriptomes of the four samples were assembled, the makeblastdb command of BLAST v2.13.0+ was used to build a database with each transcriptome. To verify the species of origin of the samples, the predicted mRNA sequences of the *R. ferrumequinum* cytochrome c and cytochrome b genes (XM_033088428.1 and XM_033112251.1 respectively) were used. The cytochrome c gene and the cytochrome b gene have been used in species identification studies previously.[13,73] With these sequences in FASTA format, searches were made with the blastn command of BLAST v2.13.0+ in the four databases generated with the transcriptomes, resulting in various contigs for each sample. To verify these results, the contigs identified by BLAST with the highest score and the lowest E-value for each gene and each sample were extracted from the assembled transcriptomes using seqtk.[74] With these contigs, the complete nt database of the NCBI BLAST website was searched to verify that the samples came from *R. ferrumequinum*.

RaTG13 annotation and plasmid cloning

RaTG13 (MN996532.2) genome sequence was downloaded from GenBank and utilized to design 2xStrep-tagged expression constructs of ORFs and proteolytically mature Nsps derived from ORF1ab (with N-terminal methionines and stop codons added as necessary). SARS-CoV-2 and RaTG13 reading frames were codon-optimized for mammalian expression and cloned into pLVX-EF1alpha-IRES-Puro (Takara/Clontech) or pLVX-TetOne-Puro (Clontech) including a 5′ Kozak motif with either N-terminal or C-terminal 2XStrep tags using EcoRI and BamHI restriction sites. Similarly, human and bat host protein sequences were codon-optimized for *Homo sapiens* expression and inserted into pcDNA 3.1 vector (Addgene) with a C-terminal Flag-tag using HindIII and BamHI

Please cite this article in press as: Batra et al., Coronavirus protein interaction mapping in bat and human cells reveals network rewiring governing immune evasion and zoonotic potential, Cell Host & Microbe (2026), https://doi.org/10.1016/j.chom.2026.04.015

restriction sites. Restriction digestions were performed at 37°C for 1 hour, followed by T4 DNA ligase-mediated ligation at room temperature for 2 hours. The resulting constructs were transformed into chemically competent Stellar E. coli cells (Takara) for plasmid propagation.

Transfection in HEK293T cells for AP-MS studies

HEK293T cells were transfected with RaTG13 viral protein constructs, along with a GFP control and a vector-only control (pLVX-EF1α-IRES-Puro), in three independent biological replicates for affinity purification. Ten million HEK293T cells were plated per 15-cm dish. Twenty-four hours later, cells were transfected with a total of 15 μg DNA per dish. The amount of bait plasmid used was based on prior SARS-CoV-2 affinity purification experiments12, considering relative expression levels and toxicity. Total DNA was adjusted to 15 μg with empty vector. The following amounts of bait plasmid were transfected per dish: 0.5 μg GFP; 3 μg Orf3a, Nsp14; 6 μg M; 7 μg Orf7b, Orf9c, Nsp5, Nsp6; 10 μg Nsp4, Nsp12, S; 15 μg N, Nsp1, Nsp2, Orf3b, Orf7a, Orf7b, Orf9b, Orf9c, Orf10, Nsp13, Nsp15, and empty vector. DNA was complexed with PolyJet Transfection Reagent (SignaGen Laboratories) at a 1:3 μg:μl ratio of DNA to transfection reagent, following the manufacturer's instructions. After >40 h, cells were harvested using 10 ml DPBS without calcium or magnesium, supplemented with 10 mM EDTA for ∼5 minutes, followed by three washes with 10 ml DPBS. Each step was followed by centrifugation at 200 g for 5 min at 4 °C. Cell pellets were flash-frozen on dry ice and stored at −80 °C.

Transduction in RFe cells for AP-MS studies

For lentiviral transduction, 0.5 million RFe cells were spinoculated with 400 μl of concentrated lentivirus in the presence of 8 μg/ml polybrene by centrifugation at 1,000 × g for 1 hour at room temperature. Transduced cells were then transferred to a T75 flask for recovery. Four days post-infection, cells were selected with 2.5 μg/ml puromycin until non-transduced control cells were completely dead. Following expansion, 10 million cells per 15-cm dish were seeded for affinity purification, with two dishes per sample in triplicate. The following day, doxycycline was added at 1 μg/ml to induce expression. Cells were harvested >24 hours after doxycycline induction. Cells were washed twice with cold DPBS, scraped in cold DPBS, and the suspensions were centrifuged at 200 × g for 5 minutes at 4 °C. Supernatants were removed, and cell pellets were snap-frozen on dry ice and stored at -80 °C.

Sample preparation for AP-MS studies

Frozen cell pellets were thawed on ice for 10-15 minutes and resuspended in 1 ml IP lysis buffer (50 mM Tris-HCl, pH 7.4 at 4 °C; 150 mM NaCl; 1 mM EDTA), supplemented with 0.5% Nonidet P40 substitute (NP40; Fluka Analytical), cOmplete™ mini EDTA-free protease inhibitor cocktail, and PhosSTOP™ phosphatase inhibitor cocktail (Roche). Samples were incubated on a tube rotator at 4 °C for 30 minutes, frozen on dry ice for 20–25 minutes, partially thawed at 37 °C, and then fully thawed on ice. This freeze-thaw cycle was repeated once, followed by centrifugation at 13,000 g for 15 minutes at 4 °C to pellet cell debris. 40ul of Clarified cell lysates was mixed with SDS loading buffer for expression analysis by western blotting using the indicated antibodies. Up to 96 clarified lysates were arrayed into a 96-well deep-well plate for automated affinity purification using the KingFisher Flex (KFF) Purification System (Thermo Scientific) in the cold room. MagStrep 'type3' beads (40 μl; IBA Lifesciences) were equilibrated twice with 1 ml wash buffer (IP buffer with 0.05% NP40), and incubated with 0.95 ml lysate for 2 hours. Beads were washed three times with 1 ml wash buffer and once with 1 ml IP buffer. For on-bead digestion, beads were resuspended in 50 μl denaturation-reduction buffer (2 M urea, 50 mM Tris-HCl pH 8.0, 1 mM DTT), incubated at 37 °C for 45 minutes, and then brought to room temperature. Proteins were alkylated in the dark with 3 mM iodoacetamide for 45 minutes and quenched with 3 mM DTT for 10 minutes. Bead-bound proteins were digested overnight at 37 °C with 1 μl trypsin (0.5 μg/μl; Promega), followed by additional 0.5 μl trypsin for 2 hours. All incubation steps were performed with constant shaking at 1,100 rpm using a ThermoMixer C incubator. Resulting peptides were combined with 50 μl of 50 mM Tris-HCl (pH 8.0) to rinse the beads, then acidified with trifluoroacetic acid to a final concentration of 0.5% (pH < 2.0). Acidified peptides were desalted for mass spectrometry using a BioPureSPE Mini 96-Well Plate (20 mg PROTO 300 C18; The Nest Group) following standard protocols.

MS data acquisition and peptide search

Samples were resuspended in 0.1% formic acid and analyzed using a Q Exactive Plus mass spectrometer (Thermo Fisher Scientific) coupled to an Easy-nLC 1200 ultra-high-pressure liquid chromatography (UHPLC) system via a Nanospray Flex nanoelectrospray ion source. Peptides were loaded onto a C18 reverse-phase column (25 cm × 75 μm, packed with ReproSil-Pur 1.9 μm C18 resin). Analytical columns were equilibrated with 5 μl of mobile phase A with a max pressure of 650 bar. HPLC buffer A consisted of 0.1% FA, and buffer B consisted of 0.1% FA / 80% ACN. Peptides were eluted by a linear gradient from 7 to 36% B over the course of 53 min at a flow rate of 300 nL/min, after which the column was washed with 95% B and re-equilibrated at 2% B. Each sample was analyzed with a 75-min acquisition, with all MS1 and MS2 spectra collected in the orbitrap in positive ion mode. MS1 scans were collected in profile mode with 70,000 resolving power, a $1x10^6$ AGC setting, 250ms maximum injection time, and a scan range of 300 - 1500 m/z. MS2 scans were collected in centroid mode with 17,500 resolving power, a $5x10^4$ AGC setting, 60ms maximum injection time, a 2.0 m/z isolation window, a normalized collision energy of 26, a loop count of 20 MS2 scans, a minimum AGC target of $8x10^3$, an intensity threshold of $1.3x10^5$, exclusion of unassigned and z=1 charge states, automated dynamic exclusion timing, and a scan range of 200 - 2000 m/z. Data was acquired using the Thermo software Xcalibur (4.2.47), Tune (2.11 QF1 Build 3006), and instrument suitability was monitored by QCloud.[75] For HEK293T samples, proteomic data were searched using MaxQuant

(v1.6.12.0)[76] against the UniProt-reviewed human proteome (downloaded February 28, 2020), enhanced green fluorescent protein (EGFP), and SARS-CoV-2 or RaTG13 protein sequences. Similarly, *Rhinolophus ferrumequinum* protein sequences were downloaded from UniProt and NCBI. To remove redundancy, sequences were grouped by Ensembl gene ID, and the longest sequence within each group was selected. Only sequences that appeared in both UniProt and NCBI were retained. RFe data were searched against this curated *Rhinolophus ferrumequinum* proteome, along with EGFP and SARS-CoV-2 or RaTG13 sequences. All raw MS data and search result files have been deposited in the ProteomeXchange Consortium via the PRIDE[59] repository (PXD identifier: PXD065873).

Ortholog mapping of RFe proteins and percent identity

Orthologous gene pairs between *Rhinolophus ferrumequinum* and *Homo sapiens* were downloaded from Ensembl using the BioMart web interface (https://useast.ensembl.org/biomart/martview/b6f5f7374d580d6789a559a40e68a515). Ensembl gene identifiers were mapped to UniProt identifiers and corresponding protein sequences using UniProt ID mapping tables and the reference *H. sapiens* proteome. Orthologous protein sequences were aligned using the Needleman–Wunsch global alignment algorithm, implemented via the pairwiseAlignment function in the Biostrings R package (v2.52) with default parameters. Orthologous gene assignments were also compared against the InParanoid ortholog database.[77] Global alignments between *Rhinolophus ferrumequinum* and human proteins with the same gene name were performed using pairwiseAlignment from Biostrings (v2.68.1) in R. Sequence identity was calculated as 100 $\times$ (identical positions) / (length of shorter sequence). The percent identity between SARS-CoV-2 and RaTG13 viral proteins were calculated using Clustal Omega.[78]

High-confidence protein interaction scoring and DIS analysis

Identified proteins were then subjected to PPI scoring with both SAINTexpress (version 3.6.3) and MiST (https://github.com/kroganlab/mist).[14,15] High confidence PPIs were defined by a MiST score $\geq$ 0.7 and a SAINTexpress Bayesian false discovery rate (BFDR) $\leq$ 0.05. For all proteins meeting these thresholds, information on known stable protein complexes was retrieved from the CORUM database (CORUM).[20] For a subset of viral baits, specifically RaTG13 M, Nsp12, Orf8, and Orf9b in HEK293T cells, and RaTG13 M in RFe cells, we observed a substantially higher number of PPIs passing the standard thresholds. For these baits, a more stringent filtering criteria was applied: AvgSpec > 3, MiST $\geq$ 0.8, and SAINTexpress BFDR $\leq$ 0.05. We then computed a Differential Interaction Score (DIS)[18] for all interactions that passed the high-confidence criteria in at least one virus or species. The DIS was defined as the difference in interaction scores (K), calculated as the average of the MiST and SAINT scores, between the two viruses or species being compared. A DIS value near 0 indicates a shared interaction, while values approaching -1 or +1 indicate that the host–protein interaction is specific to one virus or species.

Network generation and visualization

PPI networks were generated in Cytoscape[79] and annotated in Adobe Illustrator. Host–host physical interactions, protein complex definitions, and biological process groupings were obtained from CORUM,[80] Gene Ontology[21,22] (biological process), and manually curated literature sources.

Analysis of *Rhinolophus ferrumequinum* - *Rhinolophus affinis* orthology

We downloaded all predicted *R. ferrumequinum* CDS and protein sequences from the Ensembl database (release 115; annotations derived from genome assembly, GenBank: GCA_004115265.2[81]), as well as information on how Ensembl gene, transcript and protein IDs align with Uniprot protein IDs (file Rhinolophus_ferrumequinum.mRhiFer1_v1.p.115.uniprot.tsv). This dataset contains 33,717 protein sequences from 19,533 distinct genes. We also downloaded a genome assembly for *R. affinis* (Genbank: GCA_043728065.1[55]). We used the miniprot algorithm[82] (version 0.13-r248) to perform a spliced, translated alignment of each *R. ferrumequinum* protein against the *R. affinis* genome sequence using default parameters, obtaining a gff output file, which we then used to extract predicted *R. affinis* CDS sequences. We realigned each *R. affinis* CDS sequence to the corresponding *R. ferrumequinum* CDS query sequence using the MACSE[83] frameshift-tolerant alignment algorithm (version 2.07, default parameters, except that we used an increased frameshift penalty: "-fs 80 -fs_term 80"). We then removed poorly aligning regions from the resulting nucleotide and amino acid alignments using the TrimAl[84] algorithm (version 1.5.rev0, using the " -automated1" option for automated method selection and the " -ignorestopcodon" option). We also used each *R. affinis* CDS sequence as a query in a blastn[85] search of all *R. ferrumequinum* transcript sequences, recording the identity of the best match. If the best *R. ferrumequinum* match was from the same gene as the original *R. ferrumequinum* protein query, we considered this a one-to-one orthology relationship, otherwise we considered the sequence pair to represent likely paralogs rather than orthologs. We used R and Bioconductor[86] packages to calculate ungapped protein identities and query coverage from the resulting alignments ("coverage" = trimmed and degapped amino acid alignment length, divided by length of the original protein sequence). We selected a single protein isoform for each gene for the plots, using the gene-to-protein linkages provided by Ensembl, prioritizing one-to-one orthologous isoforms, then choosing based on the highest miniprot score (breaking any ties by the highest blastn score).

Deep proteome profiling

The SP3 digest method was done similarly as described in Hughes et al.[87] Cell pellets were thawed on ice and mixed with 1 ml of lysis buffer consisting of 50 mM HEPES pH 8 (Thermo Fisher Scientific #J63578AP), 1% (wt/vol) SDS (Sigma-Aldrich #L3771), 1% (vol/vol)

Please cite this article in press as: Batra et al., Coronavirus protein interaction mapping in bat and human cells reveals network rewiring governing immune evasion and zoonotic potential, Cell Host & Microbe (2026), https://doi.org/10.1016/j.chom.2026.04.015

Triton X-100 (Sigma-Aldrich #T9284), 1% (vol/vol) NP-40 (Sigma-Aldrich #74385), 1% (vol/vol) Tween 20 (Sigma-Aldrich #P7949), 1% (wt/vol) deoxycholate (Sigma-Aldrich #D6750), 5 mM EDTA (Corning #46-034-CI), 50 mM NaCl (Sigma-Aldrich #S7653), 1% (vol/vol) glycerol (Sigma-Aldrich #15523), and 1 cOmplete protease inhibitor (Sigma #04693132001) (per 5 ml). Lysates were sonicated for 5s at 10% magnitude three times and centrifuged at max speed (13,000 rpm) for 5 minutes to pellet any insoluble material. The supernatant was then transferred to new Protein lo-bind tubes. Protein quantification was then performed by 660 assay (Thermo Fisher Scientific #22660) with ionic compatibility reagent (Thermo Fisher Scientific # 22663). 3.5 mg of each sample was transferred to new tubes. 100 mM Tris (2-carboxyethyl) phosphine (TCEP) (Thermo Fisher Scientific # 77720), 400 mM 2-chloroacetamide (Sigma-Aldrich #C0267) was added at 1:10 volume to each sample, and set in a Thermo Mixer to shake at 1,200 rpm at room temperature for 30 minutes. To prepare Sera-Mag bead solution for protein binding, SP3 beads (GE Healthcare, #45152105050250 and 65152105050250) were set at room temperature to warm. Beads were resuspended by pipetting, then equal parts of resuspended beads were combined into a slurry, with 350 μl bead solution added to each 3.5 mg reaction (4.5 ml of each bead type). Tubes were set on a magnetic rack and allowed beads to aggregate. Supernatant was removed and the beads were washed with 2x starting volume with water (700 μl per reaction, 18 ml total) three times. Supernatant was then removed, and the beads were resuspended at a concentration of 50 μg/μl. Beads were added to lysates at 1:10 weight of Sera-Mag bead solution to lysate (350 μl for 3.5 mg) to each, which were then resuspended by pipetting. Equal volumes of 100% ethanol were added to each sample for a final volume of 50% lysate, 50% ethanol. Tubes were set in a thermo mixer at 24°C for 10 minutes, shaking at 1,000 rpm. After mixing, samples were set in a magnetic rack, allowing beads to aggregate, after which the supernatant was removed and discarded. Protein bound beads were then washed three times with ~1 ml 80% ethanol, removing all the supernatant between rounds. Beads were resuspended in 400 μl 50 mM Triethylamonium bicarbonate (TEAB) (Sigma-Aldrich # T7408). Trypsin (Promega # V5111) and lysC (Wako #125-02543) were added at a 1:100 ratio enzyme to protein. Samples were then set in a thermo mixer at 37°C shaking at 1,000 rpm overnight. The following morning, supernatant was transferred to a 15 ml falcon tube, and 300 μl washed Sera-Mag bead solution was added to each followed by 10 ml acetonitrile to induce peptide binding. Samples were vortexed and set in a magnetic rack. The supernatant was then discarded. Samples were washed with 5 ml 96% acetonitrile twice, then resuspended in 1 ml 96% acetonitrile and transferred to a 1.5 ml protein lo-bind tube. Samples were set in a magnetic rack, supernatant was removed and discarded. Samples were then fractionated as reported previously.[88] Samples were sequentially eluted using isopropanol water gradients off the SP3 beads. Briefly, samples were resuspended in 800 μl 95% isopropanol, set in a magnetic rack and the supernatant transferred to a new protein lo-bind tube. This was then repeated with 90%, 85%, 80%, 75% and 70% isopropanol elutions into separate tubes. There was a final wash of water at the end to remove all remaining peptides from beads. Samples were then set in a speed-vac to dry down overnight. Prior to running on the mass spectrometer, samples were resuspended in 15 μl 2% acetonitrile, 0.1% formic acid and quantified by A205 with a 31 adjustment. Samples were adjusted to ~500 ng/μl, with 1 μl run on the instrument column.

Digested samples were analyzed on an Orbitrap Exploris 480 mass spectrometry system (Thermo Fisher Scientific) equipped with an Easy nLC 1200 ultra-high pressure liquid chromatography system (Thermo Fisher Scientific) interfaced via a Nanospray Flex nanoelectrospray source. For all analyses, samples were injected on a C18 reverse phase column (25 cm × 75 μm packed with ReprosilPur 1.9-μm particles). Analytical columns were equilibrated with 6 μl of mobile phase A with a max pressure of 650 bar. Mobile phase A consisted of 0.1% formic acid (FA), and mobile phase B consisted of 0.1% FA / 80% acetonitrile (can). Peptides were separated by an organic gradient from 4% (2%) to 30% (25%) mobile phase B over 62 min followed by an increase to 45% (40%) B over 10 min, then held at 95% B for 8 min at a flow rate of 300 nl min−1. Data-independent analysis (DIA) was performed using an 80-minute gradient. An MS1 scan at 60,000 resolving power over a scan range of 350–1100 m/z, a normalized AGC target of 300%, and an RF lens setting of 40%. This was followed by DIA MS2 scans at 15,000 resolving power, using 20 m/z isolation windows over 350–1100 m/z at a normalized HCD collision energy of 30%. Loop control was set to All. Data was then searched using DirectDIA in Spectronaut v. 16.0.220606.53000 (Hawking) by searching against a database of Uniprot Homo sapiens sequences (downloaded 22 March 2022) and a *R. ferrumequinum* proteome using Biognosys (BGS) settings, variable modifications of methionine oxidation and N-terminal acetylation, and a fixed modification of carbamidomethyl on cysteine residues. Filtering was set to a final 1% false discovery rate (FDR) at the peptide, peptide spectrum match (PSM) and protein level, with no data normalization performed. Quantitative analysis was performed in the R statistical programming language (v.4.1.3). Initial quality control analyses, including inter-run clustering, correlations, principal component analysis (PCA), peptide and protein counts and intensities were completed with the R package artMS (v. 1.12.1). Statistical analysis of protein abundance changes between conditions were computed using peptide ion fragment data output from Spectronaut and processed using artMS. MSstats performs normalization by median equalization, no imputation of missing values, and median smoothing to combine intensities for multiple peptide ions or fragments into a single intensity for their protein group.

Orf9b PPI and MSstats analysis

To quantitatively compare the PPIs of SARS-CoV-2 and RaTG13 Orf9b in HEK293T and RFe cells, we performed a separate AP-MS experiment. Cell pellets were collected for both Orf9b constructs and controls (empty vector and GFP) and processed for AP-MS as described above, with the exception that data was collected on an Exploris 480 mass spectrometer (Thermo Fisher Scientific) coupled to a Vanquish Neo ultra-high-pressure liquid chromatography (UHPLC) system via a Nanospray Flex nanoelectrospray ion source. Peptides were resuspended in 0.1% formic acid and loaded onto a PepSep C18 reverse-phase column (15 cm × 150 μm, packed with ReproSil-Pur 1.5 μm C18 resin). HPLC buffer A consisted of 0.1% FA, and buffer B consisted of 0.1% FA / 80% ACN. Peptides were eluted by a linear gradient from 2 to 28% B over the course of 32 min at a flow rate of

Please cite this article in press as: Batra et al., Coronavirus protein interaction mapping in bat and human cells reveals network rewiring governing immune evasion and zoonotic potential, Cell Host & Microbe (2026), https://doi.org/10.1016/j.chom.2026.04.015

600 nL/min, after which buffer B was increased to 44% over the course of 18 min, and finally the column was washed with 90% B and re-equilibrated at 2% B. Each sample was analyzed with a 60-min acquisition, with all MS1 and MS2 spectra collected in the orbitrap in positive ion mode. MS1 scans were collected in profile mode with 120,000 resolving power, a 100% normalized AGC setting, automatic maximum injection time, and a scan range of 350 - 1250 m/z. MS2 scans were collected in profile mode with 15,000 resolving power, a 200% normalized AGC target, automated maximum injection time, a 1.3 m/z isolation window, a normalized collision energy of 30, exclusion of unassigned and inclusion of charge states z = 2-6, and dynamic exclusion within +/- 10ppm for 30 s after 2 observations. Data was acquired using the Tune (4.2 SP4). Proteomic data were searched using MaxQuant for both HEK293T and RFe samples. We used the artMS package (v1.18.0) in R to quantify changes in "prey" protein abundance between RaTG13 Orf9b WT and SARS2 Orf9b WT. The artmsQuantification function was used with default settings, except for MBimput = 0 and normalization_method = FALSE. All raw MS data and search result files have been deposited in the ProteomeXchange Consortium via the PRIDE repository[59] (PXD identifier: PXD065873).

Network propagation

To investigate the connectivity between host proteins targeted by SARS-CoV-2 and RaTG13 proteins, we conducted a network propagation analysis. For the initial seed sets, we combined all identified prey proteins from our AP-MS experiments for each virus and propagated these seed nodes independently (16 total baits). The base network was the Reactome Functional Interactions (FI) network.[89] Network propagation was simulated using random walk with restart (RWR) to allow the initial signal from the seed proteins to spread across the network. A restart probability of 0.2 was used to balance exploration of the network while retaining influence from the initial seed nodes. We performed 20,000 simulations for each propagation to control for node degree bias. During each simulation, the labels of the seed proteins were randomly shuffled across the network to generate a null distribution. An empirical p-value was then calculated by determining the proportion of random propagation runs that produced a score greater than or equal to the observed propagation score for each node for the random propagations. Genes that were significant in either the SARS-CoV-2 or RaTG13 propagations were retained for downstream analysis. Additionally, to assess the connectivity of individual viral proteins, we performed separate network propagations for each SARS-CoV-2 and RaTG13 viral protein. For these analyses, the preys of each viral protein served as the initial seed set. Bait proteins with < 3 prey for either virus were excluded, resulting in the removal of 4 baits (Nsp1, Nsp5, Nsp14, S). The propagation was conducted the same as above with 20,000 simulations to account for network biases.

Gene set overrepresentation analysis (GSOA) was performed using the enricher function from the clusterProfiler package (version 3.12.0) in R with default parameters. For each analysis, significant GO terms (adjusted p-value < 0.05) were identified and refined to remove redundancy by constructing a GO term tree using pairwise distances calculated as 1 minus the Jaccard Similarity Coefficient of shared genes in GO Biological Process from MSigDB. The dendrogram was then cut at a height of 0.5 to define clusters of non-redundant gene sets. Within each cluster, the most significant term (i.e., lowest adjusted p-value) with the largest associated gene set was selected to ensure broad functional representation.

For the Orf9b subnetwork, we first isolated GO terms, and all associated genes, associated with "mitochondria" from the set of significant genes obtained from the initial, virus-wide, propagation results, found for either SARS-CoV-2 or RatG13. Using this gene list, we extracted a subnetwork of these genes from the Reactome FI network. This approach allowed us to focus on the functional relationships/interactions specific to mitochondrial pathways and evaluate their connectivity in the context of Orf9b across viruses.

Co-immunoprecipitation assays

HEK293T cells were transfected with the mammalian expression constructs using Lipofectamine 2000 (Invitrogen) [DNA: lipofectamine 1:1.5] according to the manufacturer's instructions. Cells were harvested in Nonidet P-40 (NP-40) lysis buffer (50mM Tris-HCl pH 7.5, 150mM NaCl, 1mM EDTA, 0.5% NP-40) supplemented with cOmplete mini protease inhibitor tablets (Roche) and PhosSTOP phosphatase inhibitor tablets (Roche). Cell lysates were clarified at 13,000 RPM for 15 minutes at 4°C. Clarified cell lysates were subjected to immunoprecipitation with anti-strep magnetic beads (IBA) with end-over-end rotation for 2 hours at 4°C, followed by 5 washes with NP-40 buffer devoid of protease and phosphatase tablets. Protein complexes were eluted from the beads by direct incubation at 95°C in 1X SDS loading buffer. Eluates and clarified cell lysates were analyzed by immunoblotting with respective antibodies.

Gaussia Princeps Protein Complementation Assay (GPCA)

HEK293T cells were transfected in 96-well plates with 100ng of each pGlc1- and pGlc2- expression plasmids. 24 h post-transfection, cells were washed once with 100µl PBS, and were lysed in 40µl of Renilla lysis buffer (#E2820, Promega) for 30 min. Gaussia princeps luciferase enzymatic activity was measured using a Berthold Centro XS LB960 luminometer by injecting 50 µl of Renilla luciferase assay reagent (#E2820, Promega) per well and counting the luminescence for 10 sec. For a given Tom70 or MTARC2/orf9b pair, 3 DNA mixtures were transfected in the same plate: (1) Tom70-Glc1 or MTARC2-Glc1 + Glc2-orf9b (2) Glc1 + Glc2-orf9b (3) TOM70-Glc1 or MTARC-Glc1 + Glc2. A Normalized Luminescence Ratio is calculated as follows: NLR = RLU (1))/ [(RLU 2) + (RLU 3)]. GPCA experiments were performed in at least 3 different cell plates, each being used to calculate a separate NLR.

Please cite this article in press as: Batra et al., Coronavirus protein interaction mapping in bat and human cells reveals network rewiring governing immune evasion and zoonotic potential, Cell Host & Microbe (2026), https://doi.org/10.1016/j.chom.2026.04.015

Innate immune sensing assay in HEK293T cells

Each viral protein was overexpressed in HEK293T cells containing a Lucia reporter under the control of the IFN-β/ISG56 promoter, alongside an empty vector control. For viral protein expression, cells were transfected with 250 ng of either empty vector or a plasmid encoding Orf9b using Lipofectamine 2000 (Invitrogen). Twenty-four hours post-transfection, cells were stimulated with varying concentrations of poly I:C. After an additional 24 hours, 20 μL of culture supernatant from each well was transferred to a white 96-well opaque plate and mixed with 50 μL of QUANTI-Luc™ 4 Lucia/Gaussia "Glow" solution (InvivoGen). Lucia activity was measured using a SpectraMax iD3 plate reader, and fold induction was calculated relative to unstimulated control cells.

Endotagging of Tom70 in RFe-AT cells and co-IP assays upon infection

Cas9/RNA ribonucleoprotein (RNP) complexes were assembled by incubating gRNA (120pmole) and Cas9 (40pmole) in appropriate electroporation buffer and incubated at room temperature for 10 minutes. The homology directed repair template (HDRT Tom70: TGCCCACGCCCAGACAGAAGTTGCAAAGAAATATGGATTAAAACCACCAACATTAATGTGGAGCCATCCACAGTTCGAAAAAGGT GGAGGTTCTGGCGGTGGATCAGGTGGAAGTGCATGGTCTCACCCTCAGTTTGAGAAATAAAATATGGGGGAAGGAAAATGACCCT CTTTTTAGAAGTTTACCCCCTCTCCAACTG) was subsequently added and incubated at room temperature for additional 5 minutes before keeping it in ice. The cells were trypsinized, washed with PBS. A total of 0.2 million cells per reaction were pelleted and resuspended in 16ul of electroporation buffer. The cell suspension was mixed with gRNA-Cas9-HDRT complex mixture and transferred to a Nucleocuvette strip. RFe-AT cells were electroporated in a P3 buffer using the pulse code EH-100. Immediately following electroporation, the cells were gently resuspended in 80 μl pre-warmed media before adding to a 6 well plate containing prewarmed media supplemented with HDR enhancer (1.7μl/2ml). Successful endotagging was confirmed by Sanger sequencing using the primers listed in the key resources table.

Endogenously 2xStrep-tagged Tom70 RFe-AT cells were mock-infected or infected with SARS-CoV-2 N_P80T or N_P80T Orf9b_T72I mutant viruses at MOI=0.5 for 48h. Cells from one 10 cm dish for each condition were harvested in Nonidet P-40 (NP-40) lysis buffer (50mM Tris-HCl pH 7.5, 150mM NaCl, 1mM EDTA, 0.5% NP-40) supplemented with cOmplete mini protease inhibitor tablets (Roche) and PhosSTOP phosphatase inhibitor tablets (Roche) and were subjected to one freeze-thaw cycle. Cell lysates were clarified at 13,000 RPM for 15 minutes at 4°C. Clarified cell lysates were subjected to immunoprecipitation with anti-strep magnetic beads (IBA) with end-over-end rotation for overnight at 4°C, followed by 5 washes with 0.5% NP-40 buffer. Protein complexes were eluted from the beads by direct incubation at 95°C in 1X SDS loading buffer. Eluates and clarified cell lysates were analyzed by immunoblotting with respective antibodies.

Co-IP assays with endogenous Tom70 in MRC5-ACE2 cells upon infection

MRC5-ACE2 cells were mock-infected or infected with SARS-CoV-2 N_P80T or N_P80T Orf9b_T72I mutant viruses at MOI=1 for 24h. Cells from two 10 cm dishes for each condition were harvested in 2ml Nonidet P-40 (NP-40) lysis buffer (50mM Tris-HCl pH 7.5, 150mM NaCl, 1mM EDTA, 0.5% NP-40) supplemented with cOmplete mini protease inhibitor tablets (Roche) and PhosSTOP phosphatase inhibitor tablets (Roche) and were subjected to one freeze-thaw cycle. Cell lysates were clarified at 13,000 RPM for 15 minutes at 4°C. Clarified cell lysates were subjected to immunoprecipitation with Anti-Orf9b and Rabbit IgG isotype control using Pierce™ Direct Magnetic IP/Co-IP Kit as per manufacturer's instructions. Briefly, 10ug of each antibody was cross-linked to 50μl of magnetic beads and were split into three tubes for IP with clarified lysates infected with SARS-CoV-2 N_P80T or N_P80T Orf9b_T72I mutant viruses or mock-infected with end-over-end rotation for overnight at 4°C, followed by two washes with IP lysis/wash buffer and one wash with ultrapure water. Protein complexes were eluted from the beads by incubation with 54μL of elution buffer at room temperature for 5 mins on a Thermomixer. Supernatants were collected in a new tube containing 6ul of neutralization buffer, followed by addition of 15ul of 5X loading buffer. Eluates and clarified cell lysates were analyzed by immunoblotting with respective antibodies.

Quantitative RT-PCR analysis

RFe cells expressing Orf9b protein from SARS-CoV-2 or RaTG13, along with vector control were seeded in 12 well plates. Next day, cells were treated with 1 μg/ml doxycycline to induce expression. At 24 h post-treatment, cells were infected with Sendai virus (SeV) and were collected 24 h post-infection in the RLT buffer. Similarly, RFe-AT and MRC5 ACE2 were seeded in 12 well plates. The next day, cells were infected with rSARS-CoV-2 N_P80T and rSARS-CoV-2 N_P80T, ORF9b_T72I viruses at MOI 0.5. At 24 and 48h post infection cells were collected in RLT buffer. RNA was extracted using the RNeasy Mini Kits (Qiagen) following manufacturer's instructions Residual plasmid DNA was removed by on-column DNase digestion using RNase-free DNase (Qiagen), followed by cDNA synthesis using SuperScript™ IV First-Strand Synthesis System (Thermo Fisher). Real-time PCR was performed using the Fast SYBR Green Master Mix (Life technologies) on a CFX Opus Real-Time PCR system (Bio-Rad), with a PCR temperature profile as follows: 95°C for 20 seconds and then 40 cycles of 95°C for 3 seconds and 60°C for 30 seconds, followed by melt curve. The expression levels of RFe MX1, ISG15, RLP13A, and human TBP, MX1, ISG15 mRNA were analyzed using gene specific primers. Expression levels were normalized to the RFe RLP13A, or human TBP house-keeping genes and mRNA copies calculated relative to mock-infected cells. Used primers are listed in the key resources table (see above).

For endogenous ACE2 and TMPRSS2 transcripts in RFe and MRC5 cells, total RNA was extracted from cell lysates using the NucleoSpin RNA II kit (Macherey-Nagel) and eluted in water. cDNA synthesis was performed on 1 μg of total RNA with RevertAid H Minus M-MuLV reverse transcriptase (Thermo Fisher Scientific) using random p(dN)6 primers (Roche). Real-time quantitative

PCR was carried out on a Quant Studio 6 Flex system (Applied Biosystems) with SYBR green PCR mix (Life Technologies) using the primers listed in the key resources table. All experiments were performed in three technical replicates. Genome copy number was inferred by extrapolation from a standard curve generated from serial dilutions of plasmids expressing human ACE2, hTMPRSS2, RfACE2 and RfTMPRSS2.

RNAseq analysis

MRC5-ACE2 and RFe-AT cells were infected with rSARS-CoV-2 WT or mutants for 24 and 48h. RNA was extracted using the RNeasy Mini Kit (Qiagen) with on-column DNase digestion, following the manufacturer's instructions. Library preparation and sequencing were performed by Azenta Life Science using the following conditions: polyA selection, standard RNAseq run in Illumina®, 2x150bp with a depth of 20 million reads per sample. Raw fastq files were downloaded from the Azenta server. Human (RefSeq assembly: GCF_000001405.40), Rhinolophus ferrumequinum (RefSeq assembly: GCF_004115265.2) and SARS-CoV-2 (GenBank: MN985325) reference genomes were downloaded from NCBI website. Read quality control, alignment and quantification were performed using the NF-core RNAseq pipeline [version 3.15].[90] Default pipeline parameters were applied unless otherwise stated. Fastp [version 0.23.4][91] was used for adapter trimming, STAR [version 2.7.9a][92] for transcriptome alignment and Salmon [version 1.10.1][93] was used for quantification. To map reads to a given host and virus species simultaneously, host and viral reference fasta and gtf files were concatenated and used as input for processing. The generated transcript-level matrices were imported into R [version 4.2.3], and summarized to gene-level counts using tximport [version 1.26.1].[94] Differential expression analysis was performed using the DEseq2 package [version 1.38.3].[95] Briefly, the DEseq2 method models gene counts using a negative binomial distribution and applies the Wald test to identify genes that are differentially expressed among the groups. Genes with an absolute log2 Fold Change >= 1 & a BH-adjusted p-value < 0.05 were considered differentially expressed. To identify enriched pathways and functional gene-sets, we used custom R scripts utilizing clusterProfiler [version 4.6.2][96] and gene ontology (GO) gene sets and KEGG pathways for enrichment. R packages ggplot2 [version 3.5.2] and ComplexHeatmap [version 2.14.0][97] were used to visualize gene counts and differential analysis results. Selected ISGs were taken from a previous study[28] and based on manual curation from the literature. All raw mRNA sequencing data files have been deposited in NCBI's Gene Expression Omnibus[98] and are accessible through GEO Series accession number: GSE302357.

RaTG13 Orf9b-hTom70 structure modeling

To assess the structural impact of sequence variation on RaTG13 Orf9b, we performed comparative modeling of the RaTG13 Orf9b bound to Tom70 using MODELLER v10.1.[99] The experimentally determined structures of the human Tom70 bound to the N-terminal domain of the SARS-CoV-2 Orf9b (PDB: 7KDT and 7DHG) served as templates. We used FoldX[100] to estimate the difference in binding affinity between the SARS-CoV-2 and RaTG13 structures.

Orf9b evolutionary studies

To investigate Orf9b evolution, we assembled a diverse set of sarbecovirus genome sequences from multiple sources. This included 69 genomes from Sallard et al.,[101] 13 additional public genomes, and 59 unique genomes from the UCSC Genome Browser.[102] To identify additional informative sequences, we performed tblastn searches of the NCBI nr database using Orf9b from SARS-CoV-2 (Wuhan-Hu-1) and RaTG13, identifying three genomes with non-reference substitutions at positions 70 and/or 72: two bat viruses (Rp22DB159 and BtSY2) and one human SARS-CoV-2 variant (MW734954.1, labeled HuCoV2-LC0020256). To expand outgroup sampling, we conducted further tblastn searches using four divergent Orf9b sequences (from Bat_Hp-betaZhejiang2013, BtBM48-31, BtBtKY72, and BtRc-o319), retaining hits with $\geq$70% identity over $\geq$200 bp and lower similarity to RaTG13 or SARS-CoV-2 (Wuhan-Hu-1) than to the outgroup query. All collected genomes were aligned using MAFFT v7.526,[103] and the region corresponding to the annotated SARS-CoV-2 (Wuhan-Hu-1) N ORF was extracted from each genome. Candidate ORFs $\geq$800 bp were retained and used to construct an in-frame nucleotide alignment with MACSE v2.07.[104] Phylogenetic reconstruction was performed with PhyML v3.3.20200621[105] using the GTR+F+I model and four rate categories. This analysis revealed a distinct clade in which an Orf9b-like overlapping ORF was conserved. We further filtered for unique N ORF sequences, reducing redundancy, and generated a final phylogeny rooted at the common ancestor of RaTG13 and BtBtKY72, following Sallard et al. Visualization of the tree and corresponding alignments was performed using the ggtree[106] and ggmsa[107] R packages. We noted that coronavirus evolutionary history is complicated by numerous recombination events.[101] While we made the tree from the N ORF, and show alignments for regions within N ORF, recombination means that this single phylogeny does not fully reflect the history of these genomes.

SARS-CoV-2 mutation frequency

We obtained time-resolved mutation frequencies of the Orf9b T72I mutation (C28498T) in human SARS-CoV-2 isolates from the CoV-Spectrum site,[108] which uses data from GISAID.[109]

QUANTIFICATION AND STATISTICAL ANALYSIS

Quantification and statistical analysis of the mass spectrometry and transcriptomics data was performed as described above. Quantification of the microscopy images was performed manually by counting single positive events in the highest dilution of the VLP

Please cite this article in press as: Batra et al., Coronavirus protein interaction mapping in bat and human cells reveals network rewiring governing immune evasion and zoonotic potential, Cell Host & Microbe (2026), https://doi.org/10.1016/j.chom.2026.04.015

stocks. Quantification of the luciferase entry assay was performed by measuring luciferase activity in Relative Light Units (RLU) using a luminometer. Quantification of western blot images was performed by densitometry in Image Lab 6.1 software (Bio-Rad). All other statistical analysis was performed using GraphPad Prism 10. All statistical details and the appropriate definition of parameters can be found in the figure legends and text. Data are presented as mean ± SD from one biological replicate with three technical replicates (n=3); the experiment was repeated in 2-3 independent biological replicates. Data points were considered significantly different if the p value was < 0.05.